Aalborg University, Department of Materials and Production

Deposition and Characterization of TiN Thin Films

1st semester

Physics and Technology specialization: Nanomaterials and Nanotechnology, NMNF1c

19.12.2025

AALBORG
UNIVERSITY

STUDENT REPORT

w/

Department of Materials and Production

Physics and Technology specialization: Nanomaterials and Nanotechnology

Fibigerstræde 14 and 16

9220 Aalborg

Title:
Deposition and Characterization of TiN Thin Films

Term:
1st semester

Project period:
03.09.2025 to 19.12.2025

Project group:
NMNF1c

Supervisor:
Kjeld Pedersen

Number of pages:
55

Finish date:
19.12.2025

Abstract:

In this project, Titanium Nitride thin films have been produced in order to create films with high reflectance in the near infrared region, particularly at a wavelength of 1070 nm. The TiN were deposited on Si(100), graphite and carbon fibers (CFs) substrates using reactive magnetron sputtering.

For the reflectance analysis spectrophotometer was utilised, where it was observed that the reflectance increased with deposition temperature. Further optimization through the reduction of process pressure led to maximum reflectance of approximately 84% on Si(100) substrates.

Atomic Force Microscopy (AFM) showed an increase in grain size and a more homogeneous surface morphology by increasing the deposition temperature.

Additionally, roughness analysis was conducted showing an overall increase in surface roughness. Energy Dispersive Spectroscopy (EDS) was used to estimate the thickness of the TiN films, where deposition rate was found to be higher at lower pressures. However it was assumed that the increased film thickness does not affect the reflectance.

Subsequently, TiN coatings were deposited on graphite substrate with the same optimal deposition parameters as for the Si(100), revealing lower reflectance compared to films grown on Si(100). Adhesion tests indicated relatively stronger interface between TiN and graphite rather than graphite itself.

Optical Microscope images showed that TiN was deposited successfully on CFs, however adhesion tests were inconclusive.

Contents

Preface

Ewa Wronka
ewronk25@student.aau.dk

Adriana Ago
aago25@student.aau.dk

Abdiasis Maalin Osman
aosman22@student.aau.dk

19.12.2025

Introduction 1

1.1 Introduction

Nowadays the demand for strong, lightweight, corrosion resistant composite coating materials is increasing throughout various industries, such as defense, automotive or aerospace. Carbon fibers (CFs) are preferable materials for achieving superior strength and stiffness, while maintaining the constructions lightweight. Nevertheless, their low thermal stability, together with low fracture toughness and wear resistance, reduces their effectiveness in applications where impact loading or abrasive stresses are present [1].

To overcome these limitations the so called Metal Matrix Composites (MMCs) are becoming of importance, in which metal or alloy being the main material is strengthened by for instance fibers. These MMCs display superior tensile strength, stiffness, wear resistance, yield strength, thermal stability, and low density [2]. Due to several advantages Selective Laser Melting (SLM) method is used to produce MMCs, mainly for metals such as Al and Ti. However, it depicts some disadvantages as well, which prevents it from direct application on CFs [3]. For instance, during SLM process, CFs are being exposed to high temperatures and direct laser irradiation, which significantly reduces its tensile strength [1] [4]. Another obstacle is that CFs exhibit very poor wettability with molten metals (e.g aluminum) at typical processing temperatures due to their low chemical reactivity. Although wetting improves at higher temperatures, the reaction between Al and C leads to the formation of brittle aluminum carbide, which causes interfacial degradation and is therefore undesirable [4] [5].

A viable approach to overcome these problems is the deposition of thin coatings on CFs made of metallic or ceramic layers. One material, which is widely used as a thin film is titanium nitride (TiN) due to its high hardness, temperature stability and its ability to reflect at wavelengths in the near-infrared (NIR) region. This study focuses on the specific wavelength, namely 1070 nm as it is the wavelength of the selected laser for MMC production [6] [7]. Additionally, TiN has relatively low thermal conductivity of 19.2 $Wm^{-1}K^{-1}$, which decreases the heat flux from the melt pool into the CFs. There are two techniques for thin films deposition, namely physical vapour deposition (PVD) and chemical vapour deposition (CVD) [8].

CVD technique involves high processing temperatures, varying from 800°C to 850°C, whereas CFs begin to degrade above temperatures of approximately 300°C to 400°C [1]. PVD operates under lower temperatures, therefore it is preferable method for the coating of CFs. Moreover, usually during PVD, vacuum is created in the chamber, which prevents any elements and impurities from interacting with the film [9]. There are various methods of PVD and the main

concern of this project is reactive magnetron sputtering.

1.2 State of the Art

The growing use of micro scale components has increased the interest in advancing micro and nanotechnologies in the present. Before such components can be implemented in practical applications, their surfaces often require enhancement. Improving the surface characteristics ensures that the material performs efficiently and reliably. Among the various approaches available, thin film deposition techniques offer one of the most effective solutions for addressing surface related challenges, with PVD being a well established one for the last 100 years with continuous technological advancements [10].

In 1852, Grove and colleagues first observed sputtering as what they described as a "dirt effect." At that time, achieving sufficiently low vacuum pressures for reliable film deposition was difficult, which limited practical use. It took nearly a century before sputtering saw widespread application. Today, however, technological progress and improved equipment have made sputtering a widely adopted industrial technique, capable of depositing even high melting point materials with ease [10].

In recent years, attention toward protective coatings for carbon-based reinforcements has focused on refractory nitrides such as TiN, because of their high hardness, ability to resist chemical reaction and change while remaining stable and unreactive with other compounds or environments, in addition strong thermal stability, etc. [10]. TiN has been widely performing as an effective diffusion barrier and high temperature protective layer in microelectronics, cutting tools, and composite interfaces, and continues to be investigated for advanced metal matrix composites, where fibre weakening during melt processing and additive manufacturing remains a major challenge.

To coat thermally sensitive substrates such as CFs, the field has shifted away from high temperature deposition routes like CVD in favor of low temperature PVD magnetron sputtering. Modern sputtering approaches can produce dense, stoichiometric TiN films, while preventing thermal damage of CFs and avoiding the formation of carbide at the interface. The development of reactive sputtering with improved plasma control has also increased the chances of film uniformity and reduced oxygen incorporation, both essential for achieving reliable mechanical and optical performance [1] [8] [9].

A growing research focus concerns the optical behavior of TiN, specifically its wavelength dependent reflectance. Because TiN acts practically like a metal in the NIR range, it is being investigated for plasmonic coatings, thermal protection layers and energy efficient optical components. Recent studies show that factors such as film stoichiometry, grain size and thickness strongly influence NIR reflectivity, motivating studies on process parameter optimisation in magnetron sputtering to tune these optical properties.

Parallel to this, several studies have investigated TiN as a thermal barrier coating for laser based additive manufacturing of MMCs. Its relatively low thermal conductivity helps reduce

heat transfer into CFs during laser exposure, and thereby lightening degradation during SLM. This makes TiN a promising interfacial coating for fibre reinforced MMCs produced by Laser Power Based Fusion (LPBF), where issues such as fibre damage, poor wetting, and carbide formation remain significant obstacles [8].

1.3 Problem Statement

The goal of this project is to produce TiN films with high reflectance in the NIR region in order to protect CFs during the SLM process. Si(100) and graphite substrates will be used as a model for optimisation of the TiN films to eventually be deposited on CFs. Spectrometry, AFM and EDS will be used to characterize the TiN films.

Theory 2

2.1 Titanium Nitride

2.1.1 Structure of Titanium Nitride

Titanium nitride is known for its hard and wear-resistant nature. The most known crystal structure of TiN is its rock salt-like structure, with a unit cell consisting of 4 Ti atoms and 4 N atoms. Each Ti atom is surrounded by 6 N atoms, and similarly for the N atoms as well. The structure can be viewed as two intersecting face-centered cubic (FCC) lattices. Figure 2.1 shows an illustration of the crystal structure of TiN[11].

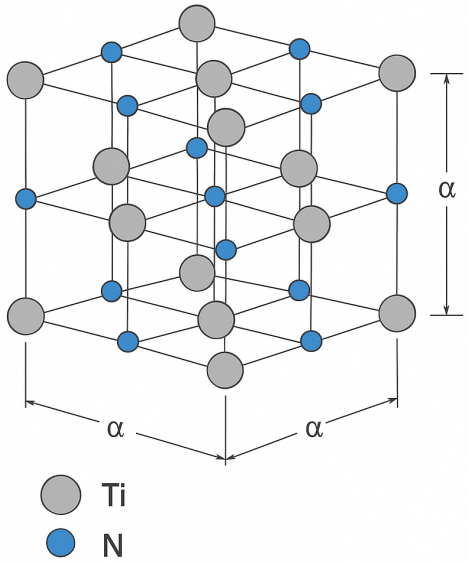

Figure 2.1: *Illustration of TiN FCC crystal structure, inspired by [11].*

2.1.2 Optical properties of Titanium Nitride

Electronic Structure

The electronic structure of TiN is governed by hybridization of titanium 3d and nitrogen 2p orbitals. some studies show that the states a few electron volts below the Fermi level are primarily composed of hybridized N 2p and Ti 3d states. At higher energies, the band mainly consists of Ti 3d states that extend through and above the Fermi level, which means the bands are partially filled and therefore support free electron movement. This is the key reason for TiN's metallic behavior[12][13][14].

Drude–Lorentz Model

Because TiN has a high density of partially filled Ti 3d states at the Fermi level, low energy excitations occur within the same band, which is called intraband transitions. This means electrons move within the same band, for example when interacting with low energy light in the NIR, contributing to its reflective behavior in these wavelengths.

Under an incident electromagnetic field, these conduction electrons behave collectively like a free-electron gas, which can be described by the Drude model[12].

The Drude model for the dielectric function is given by

$$\varepsilon(\omega) = \varepsilon_\infty - \frac{\omega_p^2}{\omega^2 + i\gamma\omega}, \tag{2.1}$$

where ε_∞ accounts for the contribution of bound electrons, ω_p is the plasma frequency, the natural oscillation frequency of the electron gas, and γ is the damping[12].

Below ω_p, the real part ε_1 tends to be negative, leading to reflective metallic behavior. Above ω_p, the material behaves more like a dielectric.

However, for materials like TiN, the Drude model by itself is insufficient, because interband transitions also contribute at higher energies. For example, when interacting with ultraviolet light, electrons jump from a lower energy state to another state in a different band. The transitions mainly consist of transitions from N 2p states to Ti 3d states.

To account for both effects, a Drude Lorentz model can be used, which adds multiple Lorentz oscillators[12].

$$\varepsilon(\omega) = \varepsilon_\infty - \frac{\omega_p^2}{\omega^2 + i\Gamma\omega} + \sum_j \frac{f_j\,\omega_{0j}^2}{\omega_{0j}^2 - \omega^2 - i\gamma_j\omega}, \tag{2.2}$$

where, for the j-th Lorentz oscillator, ω_{0j} is its resonance frequency, f_j is its oscillator strength, and Γ_j is its damping [12].

It is now possible to calculate a theoretical reflectivity curve based on the Drude Lorentz model. The parameters in Eq. 2.2 were taken from Reddy et al. [15], where TiN films were grown by DC reactive magnetron sputtering on a sapphire substrate at an 800°C deposition temperature. Using two Lorentz oscillators, the extracted parameters are listed in Table 2.1, where $\omega_{L,1}^2 = f_j\omega_{0j}^2$.

ε_∞	ω_p (eV)	Γ_D (eV)	$\omega_{L,1}^2$ (eV^2)	γ_1 (eV)	$\omega_{0,1}$ (eV)	$\omega_{L,2}^2$ (eV^2)	γ_2 (eV)	$\omega_{0,2}$ (eV)
3.21	7.55	0.53	110	1.83	4.72	5.38	1.82	1.84

Table 2.1: *Drude-Lorentz parameters for TiN extracted from Reddy et al. [15].*

The dielectric function seen in Eq. 2.2 can be related to the complex refractive index as [16]

$$\varepsilon(\omega) = \tilde{n}^2(\omega),$$

where $\tilde{n}(\omega) = n(\omega) + ik(\omega)$, with n being the refractive index and k the extinction coefficient.

At normal incidence, the reflectivity $R(\omega)$ of a material can be calculated from the complex refractive index using the Fresnel equation[16]

$$R(\omega) = \left| \frac{\tilde{n}(\omega) - 1}{\tilde{n}(\omega) + 1} \right|^2 . \tag{2.3}$$

In figure 2.2 a theoretical reflectivity curve calculated from the Drude–Lorentz model and parameters listed in 2.1 can be seen. For simplicity, normal incidence is assumed.

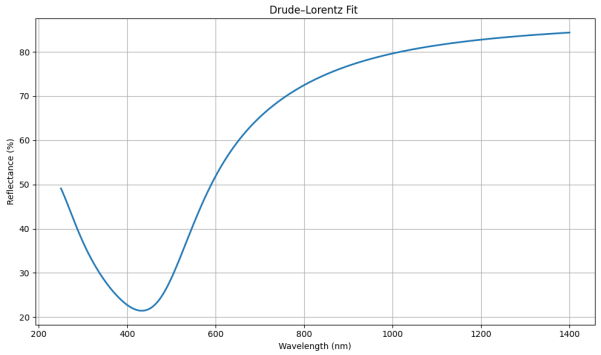

Figure 2.2: *Theoretical reflectivity curve calculated from the Drude–Lorentz model.*

This will be used in the results section.

2.2 Thin Film Growth

2.2.1 Structure Zone Model

The microstructure of TiN films can be described using the Extended Structure Zone (ESZ) model. In reactive magnetron sputtering of TiN, both the substrate temperature and the nitrogen flow strongly influence adatom mobility, leading to distinct structural zones during film growth.

Three main zones are typically distinguished for TiN, which can be seen in the Figure 2.3.

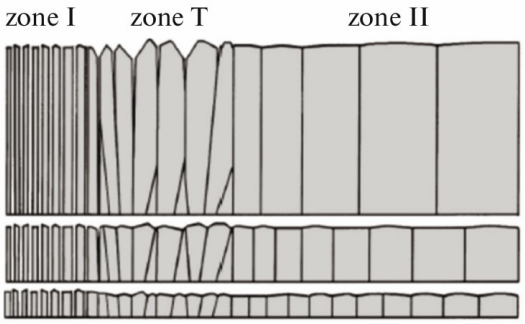

Figure 2.3: *Schematic of the structure zone model with three distinguished zones I,T,and II. Adapted from [17].*

Zone I

At low substrate temperature or low nitrogen flow, the mobility of adatoms is very limited. Particles remain close to their landing sites, resulting in a columnar microstructure with many voids. The nucleation layer is often amorphous. The film may exhibit a weak or random texture.

Zone T

With increasing nitrogen flow or slightly higher adatom mobility, the film enters the transition zone (Zone T). Here, grains begin to grow competitively, forming dense columns with pointed or pyramidal tops. For TiN, Zone T growth often results in a strong (111) texture, because (111)-oriented grains tend to grow faster under conditions where mobility is moderate but not sufficient for full recrystallization. The surface roughness increases due to the formation of grain tips.

Zone II

At higher substrate temperature or higher ion bombardment energy, surface mobility becomes sufficient for significant grain boundary movement and recrystallization. This leads to dense films with well defined columnar grains. In this regime, TiN typically adopts the thermodynamically preferred (200) orientation. The number of voids decreases and the film surface becomes more uniform[17].

2.2.2 Lattice Mismatch

Epitaxy growth is when a thin film grows on a crystalline substrate, inheriting the same crystal structure and orientation of the substrate it has grown on. Epitaxy growth can be divided into two: *homoepitaxial* growth and *heteroepitaxial* growth. In homoepitaxial growth, the thin film and the substrate are the same material, while they are different materials in heteroepitaxial growth.

In the case where the thin film material and the substrate material are different, the substrate lattice and thin film lattice are not perfectly matched. This leads to a lattice misfit, which is given by

$$\varepsilon_0 = \frac{a_s - a_f}{a_s}. \tag{2.4}$$

For Si and TiN, the lattice constants are $a_{\mathrm{Si}} = 5.43\,\text{Å}$ and $a_{\mathrm{TiN}} = 4.24\,\text{Å}$. Using the expression above, the lattice mismatch becomes 22%[18][19].

2.2.3 Stress and Strain

When lattice mismatch occurs, the unit cell of the thin film will experience elastic distortion. This kind of deformation is called strain and is defined by Equation 2.5.

$$\varepsilon = \frac{a_s - a_f}{a_f} = \frac{\varepsilon_0}{1 - \varepsilon_0}. \tag{2.5}$$

The strain describes the atomic displacement from the equilibrium position, which is caused by stress. When the lattice constant of the thin film is smaller than the substrate's, the thin film will experience compressive stress, and tensile stress will occur when the lattice constant is larger [18].

Machunze and Janssen investigated stress development in sputtered TiN films and found that thin films typically show high compressive stress, which gradually relaxes as the film becomes thicker [20].

Strain in the film can be relieved in several ways. One mechanism is surface roughening, where the thin film surface forms a series of rounded peaks and valleys. The strain is partially relaxed near the top of the peaks, thereby reducing the overall stress in the film [21]. In Figure 2.4 the illustration of surface roughening is shown.

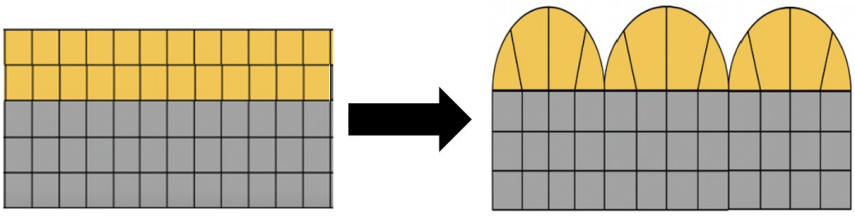

Figure 2.4: *Illustration of surface roughening inspired by [21]*

.

As the film grows thicker, relaxation through surface roughness becomes insufficient. Misfit dislocations may form at the interface when the lattice mismatch is too large. A misfit dislocation is a defect that forms at the interface between the substrate and the thin film. A dangling bond is created, originating from the substrate when $a_s < a_f$, or from the thin film when $a_s > a_f$ [21].

2.2.4 Substrate

Silicon

Selecting an appropriate substrate is essential for producing high quality thin films. In this study, TiN was deposited on silicon (100) wafers. Both Si and TiN possess cubic crystal structures and are therefore structurally compatible during growth. The (100) surfaces of both materials exhibit cubic symmetry, while the (111) planes form hexagonally arranged atomic patterns. However, in both cases, the lattice mismatch is approximately 22%, which is relatively large. This mismatch can influence strain relaxation, defect formation, and grain orientation during deposition.

Research has shown that under certain growth conditions, TiN can adopt a preferred orientation that aligns with the crystallographic direction of the silicon substrate, producing textured or partially epitaxial films [22].

Other studies, on the contrary, indicate that TiN forms a polycrystalline structure with different orientations, depending on deposition conditions such as nitrogen flow, substrate temperature, and the extent of ion bombardment during sputtering [17].

Graphite

Graphite is another substrate that can support TiN thin film growth, particularly when high deposition temperatures are required, due to the fact that it is a fully crystalline carbon material composed of stacked layers of sp^2- bonded carbon atoms, giving it excellent thermal resistance. This arrangement allows graphite in this study to withstand temperatures well over 500 °C in vacuum without undergoing structural degradation or chemical decomposition, making it a highly suitable substrate for high temperature sputtering procedures [23].

Because graphite remains stable at high temperatures, sputtering can be performed under conditions that increase the rate of surface diffusion. At higher temperatures, Ti and N atoms possess greater mobility, enabling them to reorganize on the graphite surface and form dense, well-crystalized TiN films [24].

However, TiN and graphite do not share compatible crystal lattices because TiN has a face-centered cubic crystal structure as mentioned earlier, and graphite has a hexagonal crystal structure that is layered, which does not enable some degree of structural matching during deposition [25]. As a result, films on graphite tend to exhibit greater variation in grain size and reduced uniformity [26].

Carbon Fibers

CFs are high strength materials, which are made from precursors such as polyacrylonitride (PAN), and their internal structure consists of partially aligned graphene layers [27]. Although they tolerate moderate heat, these fibers begin to experience unwanted chemical and structural changes when exposed to temperatures above roughly 550-660 °C even under vacuum [28][29]. At higher temperatures, reactions such as oxidation, shrinkage etc. might occur, all of which affect the fiber's performance negatively [28]. Deposition on fibers is typically carried out at relatively moderate temperatures, so that they remain structurally intact while the surface still receives enough thermal energy to support limited atomic movement and film formation. However, oxidation and shrinkage can occur, which can compromise the fiber's intregrity during deposition unlike silicone [28] [29].

2.3 Deposition of Thin Films

The division of science involved in the analysis and alteration of surface characteristics is known as surface engineering. It provides the tools to modify the surface and subsurface regions of materials in a controlled manner, thereby enabling them to achieve the desirable performance for specific applications. The modifications used in surface engineering range from the alteration of surface chemistry to the application of protective functional coatings. Such coatings include a wide variety of materials (e.g., metals, ceramics, polymers, and composites) that can be deposited onto similar or dissimilar substrates with the aim of enhancing the surface chemical properties while maintaining the bulk characteristics of the underlying material. Techniques related to the surface coating are vapour phase deposition (physical vapour deposition (PVD) and chemical vapour deposition (CVD)), solution state processes and fusion processes. When taking under consideration the deposition of thin films, which are by the definition below 1 micron thick, the priority is given to the PVD and CVD [30].

Due to that, the focus of this paper is concentrated on these techniques, specifically, on PVD. CVD is briefly introduced in the study, only as a comparison to highlight the suitability of PVD for the present experiment.

2.3.1 Chemical Vapor Deposition

In the CVD, the thin film layers are deposited through the series of chemical reactions, such as reduction, oxidation, compound formation and many more, under distinct processing parameters, which include temperature, input concentration, pressure, gas flow rates, and reactor geometry. By monitoring and alterating the following parameters, the chemical composition of the reaction and physical structure can be tailored [30]. There are many variants of CVD, however for this case study PVD variants are more suitable due to the high processing temperatures involved in CVD, namely around 800-850°C [31]. This high temperatures result in substantially reduced strength of the CF. A study of CVD-TiN-Coated carbon fibers showed that with a TiN coating thickness of 34 nm, a single fiber tensile strength was reduced by approximately 50% (from 3.9 GPa for uncoated fiber to around 2.2 GPa for the coated one) [1]. For this reason, the present study paper focuses only on the PVD approach, which is described in the following chapter.

2.3.2 Physical Vapor Deposition

PVD, is a genetic term often referred to as thin film coating technique, which involves physical converting of a solid material into a vapour phase by evaporation, sputtering or ion bombardment. This vapour is subsequently carried through a vacuum, low-pressure gas or plasma environment before condensing on the surface of a substrate to form a thin layer. PVD processes are typically employed to deposit films ranging in thickness from a few nanometers up to several micrometers. PVD processes can be used to deposit films of pure elements, alloys, as well as compounds through reactive deposition. In reactive deposition, the depositing material reacts

with a gas in the surrounding environment (e.g., nitrogen) to form a compound (e.g., TiN). There are various types of PVD processes, which include vacuum or thermal evaporation, arc vapour deposition, sputter deposition and ion plating [32][30]. Sputter deposition shows better results at producing coatings of compound materials and alloys [33]. Thus, sputter deposition is the main focus of this paper and it is thoroughly described in the subsequent chapter.

2.3.3 Physics of Sputter Deposition

Sputter deposition involves physical converting of a solid material into a vapour made of individual atoms or molecules. It is done through the momentum transfer from bombarding the target with accelerated ions of a gaseous material, usually Argon as it is an inert gas. [32]. To generate the charged particles needed for sputtering, a plasma must first be ignited. A simple plasma reactor contains of two parallel plates, cathode and anode, connected to a dc power supply. When a sufficiently high voltage is applied, the electric field exceeds the breakdown strength of the gas, leading to the formation of numerous ions and free electrons. The required breakdown voltage is given by the following Paschen's law:

$$V_{bd} \propto \frac{P \times L}{\log P \times L + b} \tag{2.6}$$

Where, P is the chamber pressure, L is the electrode spacing, and b is a constant [33]. The ejected electrons can now ionize further argon particles, which enables to sustain the glow discharge. After plasma is created, positively charged argon ions in the plasma are accelerated towards the negatively charged cathodic deposition material (target), ejecting (sputtering) the molecules from its surface by the transfer of momentum. While positively charged ions strike the target surface, they can release secondary electrons, which then can collide with neutral species, while being accelerated from the cathode to anode [33][34]. The possible outcomes of ions striking the target's surface is best illustrated on the Figure 2.5. When the ion particle

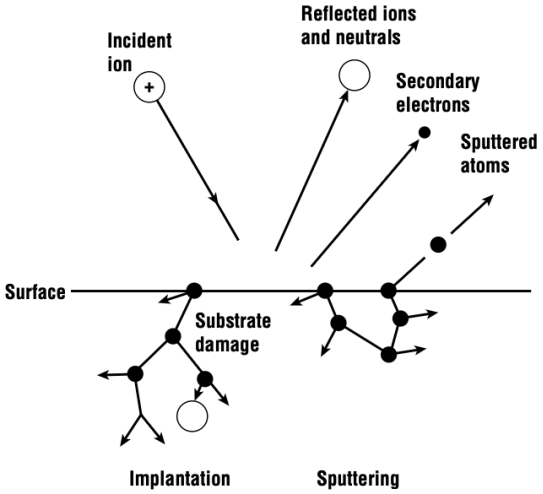

Figure 2.5: *Schematic illustration of the ion incident on the target surface. Adapted from [33]*

contains sufficient amount of energy it ejects the deposition material atom, which then moves

towards the substrate depositing thin films on the substrate [34]. Figure 2.6 depicts the overall

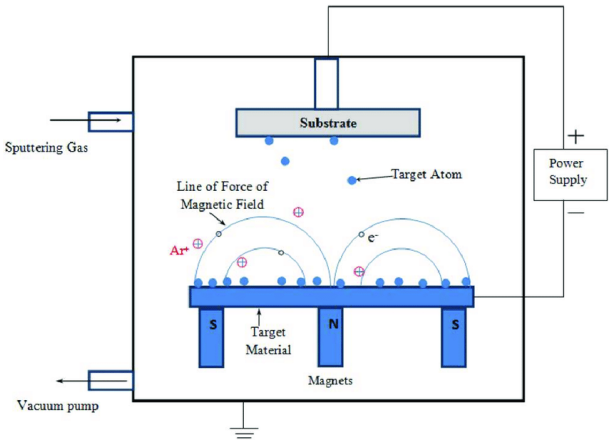

Figure 2.6: *Magnetron Sputtering deposition process. Adapted from [34]*

sputtering process. Sputtering process is a non-thermal vaporization deposition, as it requires no thermal energy, which makes it an advantageous technique widely used in industry. There are different sputtering configurations, such as Direct Current (DC), generally used for metals, and Radio Frequency (RF) potential used for nonconducting materials. Moreover, to increase the efficiency of ionization process, the magnetron sputtering technique can be distinguished [34].

2.3.4 Magnetron Sputtering

In the magnetron sputtering process, permanent magnets are attached below the target, in order to create the static magnetic field, which is parallel to the cathode (target) surface. Due to that, secondary electrons, emitted from the cathode by the ion bombardment are confined by the magnetic field so that their motion remains perpendicular to both the electric (normal to the target surface) and magnetic fields caused by the force $F = \boldsymbol{E} \times \boldsymbol{B}$ [35]. The arrangement of magnets is depicted in the Figure 2.6. As a consequence the electrons are concentrated near the target, increasing the number of collisions with gas molecules and thus improving the efficiency of the process [34]. The last modification in the sputter deposition process applied in this study is the reactive sputtering.

2.3.5 Reactive Magnetron Sputtering Deposition

PVD processes can be used to deposit not only elements or alloys but also compounds. It is done by the intentional addition of reactive gases, such as, oxygen, O_2, or nitrogen, N_2, which subsequently react with the sputtered material creating the wide variety of compound thin coatings.

This study aims to produce Titanium Nitride, TiN, thin coatings thus, the reactive gas under consideration is N_2. Consequently, the process taking place is nitridation of Titanium.

When considering reactive sputtering, partial pressure or flow of a reactive species (N_2) is an important factor for the system to work efficiently. Figure 2.7 depicts the deposition rate

(upper one) and the discharge voltage (lower one) as a function of reactive gas flow rate. At zero reactive gas flow, on the far left side of the graphs, the sputtered films are purely metallic till the reactive gas flow point, f_r, is reached. After reaching that point, the reactive gas is being absorbed by the deposited films, creating partially nitrided films. With a further increase in the reactive gas flow, the so called critical flow point f_c is reached, where the process is saturated with nitrogen. If any more reactive gas is added above this point, then the extra nitrogen will start creating a layer on the target surface, causing the decrease in sputtering yield [35].

Reaching this transition, the reactive gas flow has to be highly reduced in order to reach the efficient deposition rate. It is due to the presence of residual reactive gas layer on the cathode, which has to be cleared [35].

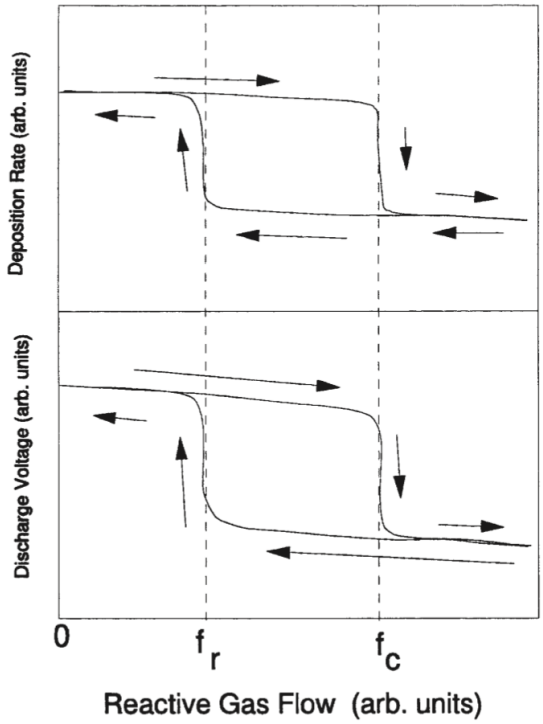

Figure 2.7: *The deposition rate (top) and the discharge voltage (bottom) as a function of reactive gas flow. Adapted from [35]*

2.4 Effect on Deposition Parameters

The deposition of thin films is a fundamental process in modern materials science, as well as in fields such as electronics, optics and nanotechnology [36].The microstructure and physical properties of the films formed - which in our case involve the TiN thin films - depend on the conditions under which the deposition has taken place. The precise control of these parameters allows tailoring of characteristics such as crystallinity, morphology, thickness, adhension and electrical conductivity, but also variations in their chemical composition, which has a great influence on the coating performance [37] [38] .The key parameters affecting thin film deposition are going to be discussed, with emphasis on Physical Vapor Deposition (PVD) and TiN thin

films.

2.4.1 Substrate Temperature

Substrate temperature is one of the most important factors influencing the structural and functional properties of a thin film, since it determines the mobility of absorbed atoms (adatoms) that is, individual atoms located on the crystal surface - during growth. Their kinetic energy is related to the energy of the argon ions and the average recoil energy of the ejected atoms [39]. At low substrate temperatures, limited diffusion at the surface leads to the formation of amorphous or very fine-grained films [36]. On the contrary, at higher temperatures the mobility of the atoms increases, facilitating their rearrangement into more crystalline structures and improving both the density and adhesion of the film [38]. In this study temperatures above 450-500 can cause diffusion between Ti and Si, which is the substrate used in this project. Furthermore, deposition at higher substrate temperature leads to nitrogen desorption and the elimination of pores and voids, which are helpful in decreasing the coating thickness and increasing the hardness.

2.4.2 Process Pressure

During deposition the mean free path length of the particles directed towards the silicon (Si) substrate is directly affected by the working pressure [36]. At low pressure conditions, the particles have higher kinetic energy, which leads to the formation of dense and compact films. In contrast, at high pressures, frequent collisions reduce the energy of the particles, resulting in the formation of more porous or columnar microstructures, which exhibit increased electrical resistance and reduced adhesion.

2.4.3 Deposition Rate and Time

Deposition rate affects both the microstructure and the uniformity of the thin films [36] [38]. A high deposition rate can lead to films with lower density and increased roughness, as the limited time does not allow the adatoms to reaarange sufficiently on the surface. In contrast, a lower deposition rate gives more time for surface diffusion - in this case between Ti and Si, resulting in smoother and denser films [40].

2.4.4 Gas Flow Rate and Composition

In reactive sputtering and CVD processes, gas flow rate and composition are vital for achieving the desired stoichiometry. The type and quantity of reactive gases, which on the present study the focus is mainly on producing Titanium Nitride coatings, the reactive gas used is N_2 and the process performed is titanium nitriding,are important due to the fact that they react with the sputtered material and form complex thin films but also determine the film's chemical composition. An optimal gas flow ensures stable plasma conditions and uniform film growth [35] .

Excess reactive gas can "poison" the target surface, reducing the deposition rate and altering stoichiometry. Since at zero reactive gas flow the films are pure metal until they reach flow point, nitrogen begins to be absorbed by the film and partially nitrided films are formed. So the further increase can saturate the process with nitrogen Conversely, insufficient gas flow of nitrogen may yield the sputtering due to the layer that is created on the target surface. When this transition occurs, the flow of the N_2 must be significantly reduced to restore the efficient deposition rate, because a thin layer remains on the cathode, which must first be removed [35] .

2.4.5 Target-Substrate Distance

The distance between the target and the substrate affects film uniformity and deposition rate [36] [41]. A shorter distance provides higher deposition rates but can lead to non-uniform thickness distribution. A longer distance enhances film uniformity and smoothness but at the cost of a lower deposition rate.

2.4.6 Target Power(in PVD)

In sputtering, the target power controls the energy of ions bombarding the target [41]. Increasing the power raises the sputtering yield, thereby increasing the deposition rate. However, higher power levels can also increase substrate heating, internal stress, and defect formation [38] [40]. In order to achieve balanced deposition rate and better film quality moderate power settings are often used.

The properties of thin films are intricately linked to the deposition parameters used during fabrication. Parameters such as substrate temperature, chamber pressure, deposition rate, substrate bias, and gas composition directly influence the film, hence the optimal control of these will enable the fabrication of high-quality films. A comprehensive understanding of these relationships provides a foundation for further research on the study.

2.5 3D Printing and Selective Laser Melting (SLM)

3D printing, or additive manufacturing, is an advanced technique that builds parts directly from digital models by depositing material layer by layer. This approach allows for the rapid fabrication of metallic components without traditional tooling, offering advantages such as design flexibility, weight reduction, and part consolidation, which are particularly valuable in the aerospace, automotive, and marine industries [42]. The primary uses of additive manufacturing include rapid tooling, rapid prototyping, producing composite components, and direct part fabrication. Every 3D printing system relies on two key elements which are the energy source and the input raw material. The raw material may be in the form of plastic or metal powder, or wire. There are plenty techniques of 3D manufacturing but some of them are similar to each other [43].

Within metal additive manufacturing, powder bed fusion is especially suited for small, complex, or low-volume parts. This technique fully melts metal powder layer by layer using a laser, producing dense, homogeneous parts with high structural integrity. The process is controlled directly from a CAD model, ensuring reproducibility, and can produce advanced structures, including, in this case, metal matrix composites reinforced with continuous CFs. However, embedding fibers introduces challenges such as degradation, poor wetting, and weak interfacial bonding due to high thermal loads.

To address these challenges, Ti6Al4V ELI (grade 23) powder can be chosen due to its favorable thermal and chemical properties [44].

Methods 3

3.1 Deposition of Titanium Nitride

3.1.1 Sample Preparation

Silicon wafers, graphite substrates, and carbon fibres were prepared prior to mounting on the Flextura 200 to ensure clean surfaces and reliable handling.

Silicon

Silicon samples were cleaned using aceton and isopropanol, followed by immersion in Milli-Q water water in an ultrasonic bath for 3 minutes to remove residual contaminants. After cleaning, the substrates were dried and placed in the Flextura sample holders shown in Figure 3.1.

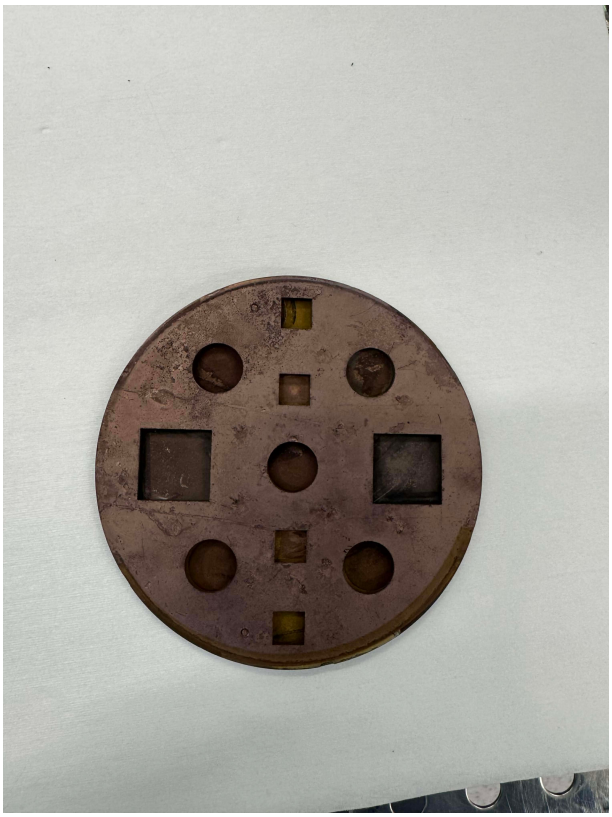

Figure 3.1: *Sample holder used to secure and align TiN before the sputtering method.*

Graphite

Graphite samples were cleaned using acetone and isopropanol. No ultrasonic treatment was applied due to the material's brittleness and softness. Once dry, they were mounted in the

appropriate sample holders used in the previous paragraph shown in Figure 3.1.

Carbon Fibers

CFs were placed directly into the sample holders as shown in Figure 3.2 without additional cleaning to avoid fibre damage or disturbance of the surface morphology. Figure 3.3 illustrates the CFs and the sample holder after the deposition.

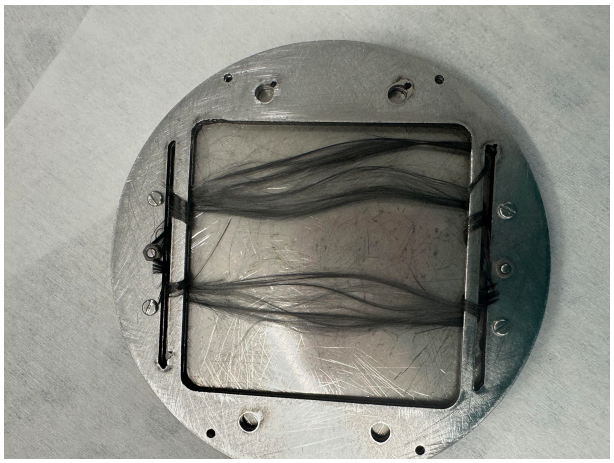

Figure 3.2: *Sample holder and carbon fibres used to deposit.*

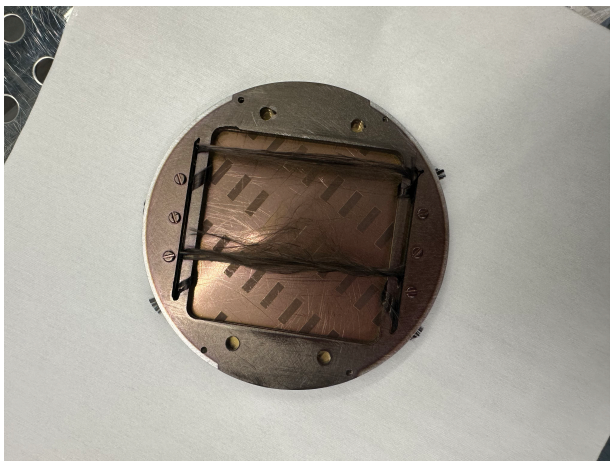

Figure 3.3: *Sample holder and carbon fibers used after the deposition.*

3.1.2 Flextura 200 Polyteknik

Thin films of TiN were grown by reactive DC magnetron sputtering in the Flextura 200 Polyteknik machine. The system used was the *Flextura 200*, which consists of four Ultra High Vacuum (UHV) chambers. A load-lock chamber (LLC), which can store up to 10 samples, a transfer chamber (TC), a sputtering chamber (SC), and an e-beam chamber.Each chamber has an attached turbo pump and is separated by gauge valves. An illustration of the Flexura system can be seen below.

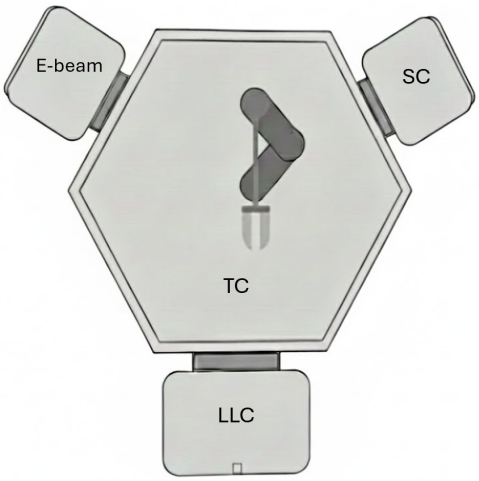

Figure 3.4: *Illustration of the flextura machine*

The substrate is loaded into the LLC. After pressing *Start*, the turbo pump for the LLC begins to run to reach the required vacuum level. When the vacuum is reached, the substrate is transported by a robot arm through the transfer chamber and into the sputtering chamber. The sputtering chamber then operates according to predetermined settings loaded from the computer connected to the Flextura system. The parameters are adjusted for each deposition.

The deposition time for all samples was set to 30 minutes. The Argon ignition flow was set to 80 sccm and applied for 60 seconds to ensure stable plasma ignition, after which it was reduced to the specified Ar flow. To remove unwanted residue from previous depositions, a 60 second pre-sputtering cleaning phase was used.

Substrate heating was also applied. The heating system allows setting a specific temperature setpoint and controlling the current. The current was set between 20–60 A, and substrates were heated to temperatures between 500–800 °C. The heating process operated with an initial heat ramp followed by a proportional–integral–derivative (PID) controller. The heat-ramp time was set to 10–25 minutes depending on the target temperature. The heat ramp brings the temperature close to the setpoint, after which the PID controller adjusts the current to heat or cool the substrate until it stabilizes within an error margin of ±10 °C. The PID current was also set to 20–60 A.

It should be noted that the temperature sensor is not in direct contact with the substrate, therefore, the actual substrate temperature may be lower than the chosen setpoint.

Below a table listing the deposition parameters for each sample is presented. The process pressure for sample 1-4 has not been recorded and is therefor unknown.

Sample	Proc. press. [mbar]	Temp. [°C]	N flow [sccm]	Ar flow [sccm]	Substrate	Dep. time [min]
1	–	500	20	15	Si(100)	30
2	–	600	20	15	Si(100)	30
3	–	700	20	15	Si(100)	30
4	–	800	20	15	Si(100)	30
5	3.9×10^{-2} mbar	800	20	30	Si(100)	30
6	1.53×10^{-2} mbar	800	10	10	Si(100)	30
7	1.52×10^{-2} mbar	700	10	10	Si(100)	30
8	1.50×10^{-2} mbar	600	10	10	Si(100)	30
9	1.53×10^{-2} mbar	800	10	10	Graphite	30
10	1.49×10^{-2} mbar	500	10	10	Carbon Fibers	30

Table 3.1: *Deposition parameters for all samples.*

3.2 Thickness Measurement

The Zeiss EVO 60 was used to estimate the thickness of the TiN thin films deposited on Si wafers, coupled to a scanning electron miscroscope.

The procedure started by preparing the sample, which is displayed on the Figure 3.5 and then choosing "vent" in the computer program, in order for the sample chamber to be under vacuum, because the electron beam would scatter in air. Selecting earthed high tension (EHT), the acceleration voltage is set to the desired value of 10kV and then the spot size is set to 500 to get the best resolution. Furthermore, to achieve the best signal-to-noise ratio, the filament current was adjusted high enough to maximize electron output without shortening the filament's lifespan, while also the electron gun was regulated so that as many electrons as possible reach the sample. A simplified view of how the electron yield and therefore image brightness, depends on filament current is shown on the figure 3.6:

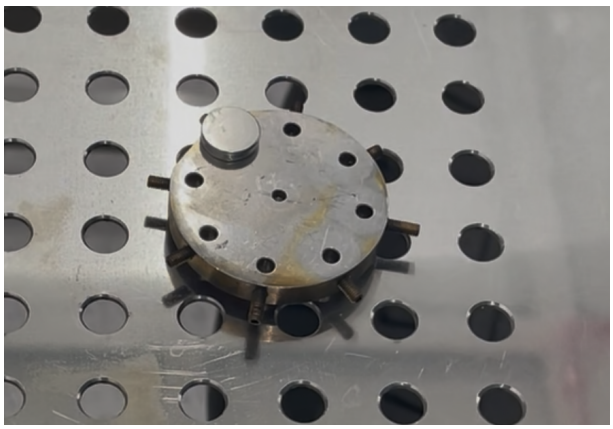

Figure 3.5: *Sample holder used to secure and align TiN before SEM imaging and EDX acquisition.*

As mentioned, to find the correct filament current, the current was increased until image brightness stopped improving (the second peak), then it was slightly reduced to protect the filament. The sample was centered and brought into focus before zooming in, and its position

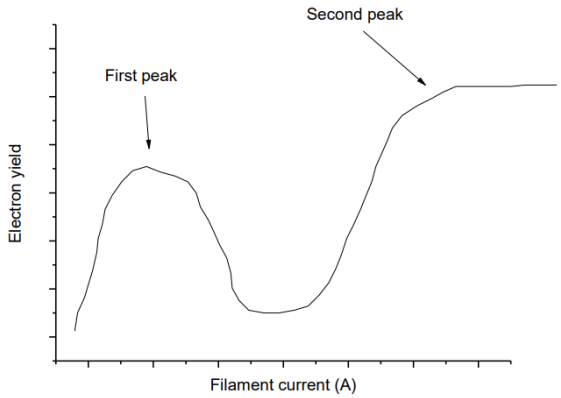

Figure 3.6: *Electron yield (image brightness) as a function of filament current, showing the first peak of maximum filament lifetime and the second peak for optimal resolution.*

was noted.

For EDS analysis, a new project folder was created and the sample height was adjusted to achieve the correct working distance. The detector settings were optimized to maintain a dead time of approximately 50–60% and total counts below 20,000 to ensure accurate energy measurement. Acquisition parameters including the maximum beam energy, low-energy cutoff, and a live time of approximately 60 s were then set, and the elements Ti, N, Si, and C were selected for analysis.

In parallel, Monte Carlo simulations were performed using CASINO v2.48. The input parameters included the accelerating voltage, takeoff angle, thin-film thickness, and the total number of simulated electrons.

The experimentally measured Ti Kα / Si Kα intensity ratio was then compared with the corresponding ratio obtained from the simulations to estimate the TiN film thickness. If a significant difference between the experimental and simulated ratios was observed, the film thickness in the simulation was adjusted iteratively until the simulated ratio either matched or was close to the experimental ratio. Measurements were also performed for different working distances, accelerating voltages, and positions on the thin film.

3.3 Reflectance Measurement

The reflectance of the TiN films was measured by the double beam, double monochromator Lambda 1050+ UV/Vis/NIR spectrophotometer from Perkin Elmer. The device provides full range of UV/Vis/NIR coverage, extending from 175 to 3300 nm. Figure 3.7 displays the schematic setup of the instrument. The device operates with D2 deuterium and a Tungsten lamp, depending on the range of measurement. The light is monochromatized by two monochromators, while the slit width determines the spectral resolution and beam intensity. A Common Beam Mask was employed, which regulates the beam cross section, ensuring that only the sample area was illuminated. Beam intensities were adjusted using attenuators, to prevent the detector from saturation or damage. Before the attenuator the beam is split into a sample beam and reference

beam, with the reference beam providing the intensity correction. Two detectors are mounted at the end, InGaAs or PhotoMultiplier Tube (PMT) detector and utilised based on the the wavelength of light [45].

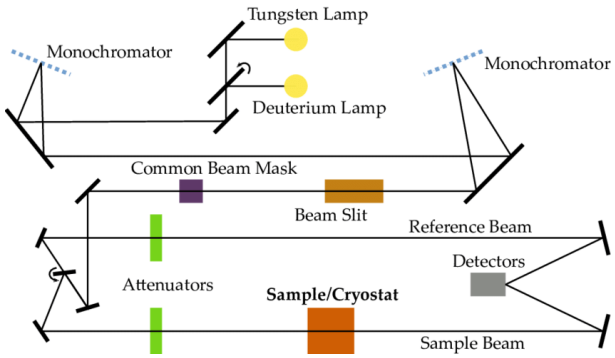

Figure 3.7: *Perkin Elmer Lambda 1050+ spectrophotometer schematic setup [45].*

For the analysis of the TiN films reflectance, both lamps were utilized, as the range of the measurements were from 1400 nm to 250 nm with data interval 3 nm. Figure 3.8 displays following settings along with other measurement parameters. In order to obtain reflectance

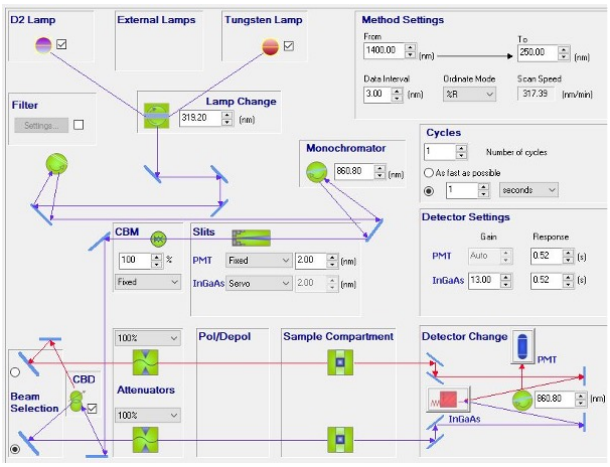

Figure 3.8: *Spectrometer settings chosen for the reflectance measurement of TiN films.*

graph, the "Ordinate Mode" was set to "%R". The slit width of the PMT sensor was set to 2 nm. Prior to the measurement of TiN sample, the instrument was calibrated for 0% reflectance by placing the certified reflectance standard from LabSphere company and choosing "Autozero" button. Figure 3.9 depicts the placement of the sample holder.

3.4 AFM

AFM measurements were carried out through the Nova PX control software. Prior to carrying out the measurements, the SPM controller, illumination lamp, monitor, and computer were powered on. The Nova PX software was then initialized to establish communication with the instrument. Figure 3.10 depicts the AFM machine.

Figure 3.9: *Sample holder for the reflectance measurement in the spectrophotometer*

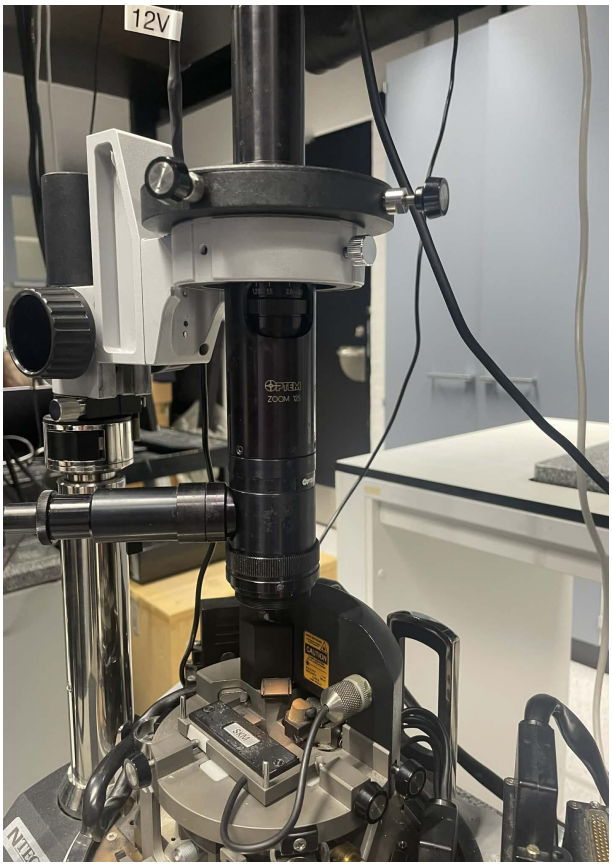

Figure 3.10: *Overview of the AFM setup used in this study.The image shows the complete instrument, including the AFM head, stage, the cantilever holder, the region where the probe is inserted, and supporting electronics.*

Because the cantilever was already installed on the AFM head, the procedure began with the cleaning of the sample holder with acetone to remove contaminants and improve adhesion and then a sticker was applied to the disk where the sample was later attached to the top surface and then placed onto the AFM stage so that its location corresponded to the center of the scanning region.

Laser alignment was carried out within the Nova PX software using the knobs located on

the AFM head, where the intensity was adjusted approximately to 30, and the cantilever was positioned so that the DFL and LF signals approached zero.

The cantilever resonance frequency was identified using the "Resonance" mode in the software. Automatic tuning was used initially, and when the resonance peak was not correctly detected, manual tuning was performed. The measured resonance frequency was confirmed to lie within the range specified by the manufacturer, which in this case was approximately 300 kHz, as shown in Figure 3.11.

Figure 3.11: *Manufacturer's packaging of the AFM cantilever used for the measurements. The label includes key specifications such as resonance frequency, cantilever dimensions etc.*

The system was switched to "Approach" mode. The "Landing" function was activated, after which the AFM automatically approached the sample surface and selected an appropriate oscillation setpoint. In order to ensure that the surface is engaging properly, the approach curves were monitored. When the approach curve displayed a smooth, gradual decrease in oscillation amplitude, this indicated that the cantilever was too far from the surface and that the van der Waals interactions were insufficient for stable imaging. In this case, the setpoint was manually reduced to increase the tip-sample interaction. In contrast, when the approach curve displayed large oscillations or instability, the setpoint was increased to prevent the tip hitting the surface of the sample. Figure 3.12 shows the software interface.

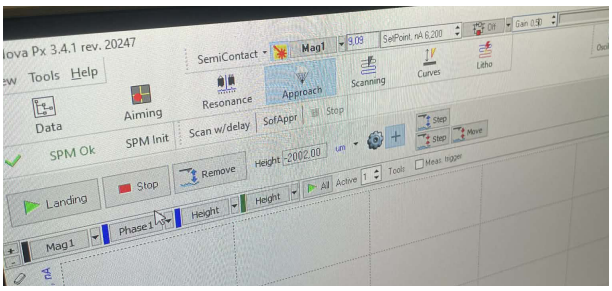

Figure 3.12: *Screenshot of the Nova PX software interface showing the Approach/Landing mode, and scanning parameters.*

Once the appropriate setpoint was found, the system was switched to "Scanning" mode. Two scan sizes were used: 2 μm x 2 μm for general surface characterization and 0.5 μm x 0.5 μm for high-resolution imaging. All scans were acquired with 512 x 512 sampling points, that provide high resolution of space. Scan parameters such as gain and scan speed were adjusted as required to maintain stable feedback and prevent imaging ruins.

Results and Discussion 4

4.1 Deposition on Si(100)

In this section, results from the deposition on Si samples are presented.

4.1.1 Reflectance

The reflectance measurements of the TiN deposited on the Si samples have been conducted as described in section 3.3.

Temperature Variation

As mentioned, one of the main goals of this project was to develop a film with high reflectance in the NIR range, especially at 1070 nm, where the Ti6Al4V powder used for SLM has high absorption at this wavelength[6] [7]. Since temperature is one of the parameters with the greatest significance in this regard, Samples 1–4 were made with deposition temperatures varying from 500–800°C, while all the other parameters remained constant as listed in table 3.1. This was done to investigate the effect of deposition temperature and to achieve a clear increase in reflectance between each deposition.

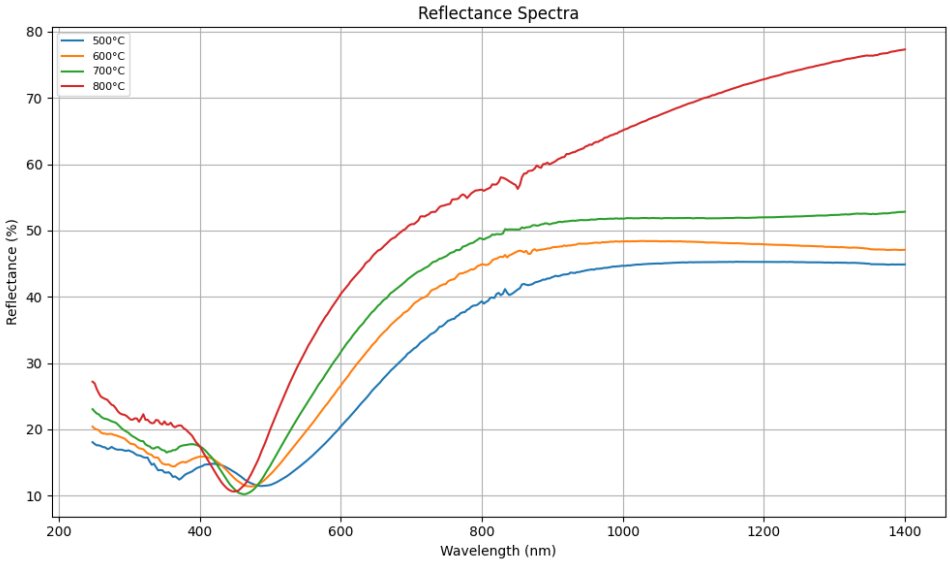

Figure 4.1: *Reflectance spectra of TiN samples 1-4*

The measured reflectances at 1070 nm can be seen in table 4.1 below.

Temp	Reflectance at 1070 [nm]
500°C	45.08%
600°C	48.38%
700°C	51.88%
800°C	67.92%

Table 4.1: *Reflectance at a wavelength of 1064 nm.*

As can also be seen in table 4.1, there is a slight increase in the reflectance at each step from 500-700°C and then a more moderate increase from 700-800°C.

The increase in reflectance with the increase in deposition temperature may be due to better crystallinity of the TiN films. Higher substrate temperatures promote grain growth, resulting in larger grains and a reduced density of grain boundaries. Since grain boundaries act as electron and photon scattering centers, their reduction leads to improved reflectance [46]. The increase in grain size with temperature is consistent with the AFM observations shown in section 4.1.2, A paper by Ma et al had the same observations as they reported that increasing the deposition temperature improved the crystallinity of TiN films and their reflectivity [47].

Gas Flow

After achieving the highest reflectance at a deposition temperature of 800°C, Samples 5 and 6 were made with varying gas flows, which indirectly changed the process pressure as well. The deposition temperature was kept at 800°C and all other parameters were held constant, besides the gas flow, in order to achieve even higher reflectance. Sample 4 is plotted together with Samples 5 and 6 for comparison, which is shown in figure 4.2.

For Sample 4, the gas flow consisted of 20 sccm N and 15 sccm Ar. For Sample 5, the gas flow consisted of 20 sccm N and 30 sccm Ar. Whereas, for Sample 6, the gas flow consisted of 10 sccm N and 10 sccm Ar.

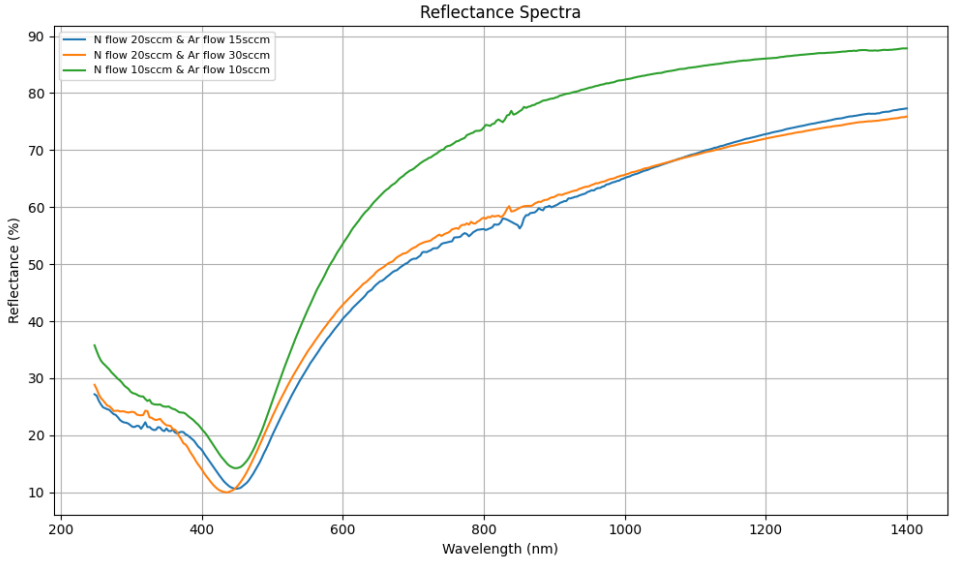

Figure 4.2: *Reflectance spectra of TiN samples 4–6. Sample 4: 20 sccm N and 15 sccm Ar. Sample 5: 20 sccm N and 30 sccm Ar. Sample 6: 10 sccm N and 10 sccm Ar.*

The measured reflectances at 1070 nm can be seen in table 4.2.

Temp	Reflectance at 1070 [nm]
800°C	67.92%
800°C	67.97%
800°C	83.87%

Table 4.2: *Reflectance at a wavelength of 1064 nm for sample*

The reflectance evidently looks unchanged between sample 4 and 5, aside from a minor variation on the minimum reflectance region. Meanwhile a higher shift can be observed on the sample 6, which is shown in figure 4.2.

It is believed that the most likely reason for the increase in reflectance is not due to a change in the gas composition itself, as can be seen for samples 4 and 5, but rather due to a decrease in process pressure. This is supported by the theory discussed in section 2.4, where lower process pressure leads to a longer mean free path, which reduces the scattering of the sputtered atoms. This increases the flux of sputtered atoms reaching the substrate surface. A longer mean free path also results in a higher deposition rate and, consequently, greater film thickness when the deposition time is kept constant, which is consistent with the thickness measurements presented later in 4.8.

However, a thicker film alone is unlikely to be the reason for higher reflectance, as TiN films are considered optically opaque at 90 nm[48]. A more likely explanation is improved microstructure as the energy of the incoming sputtered atoms would increase due to fewer collisions, which would increase the surface mobility.

After achieving a desired reflectance by finding an optimum gas composition, Sample 7 and 8 were made with lower temperature for comparison and for eventual deposition on carbon fibers. Sample 6 is plotted as well in figure 4.3 for further comparison.

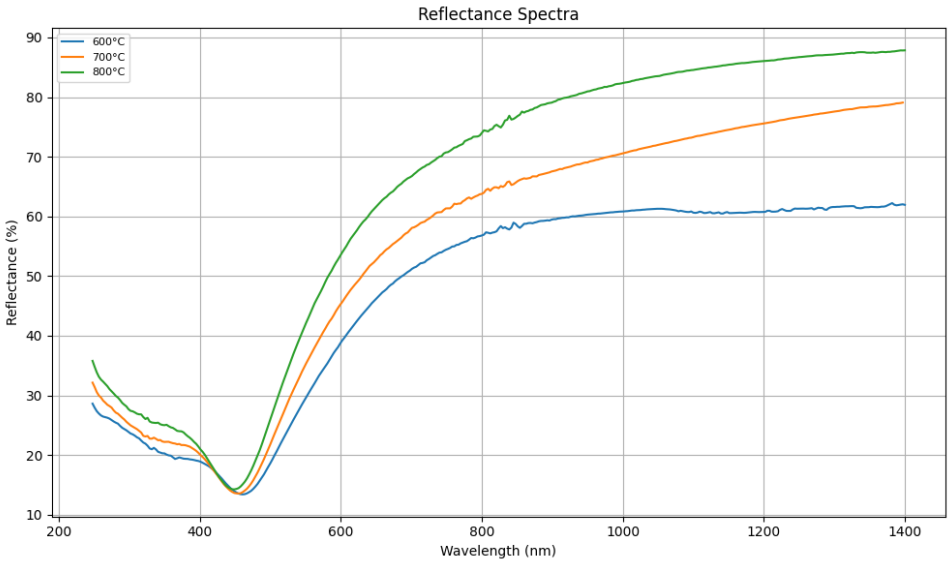

Figure 4.3: *Reflectance spectra of TiN samples 6–8 with 10 sccm N and 10 sccm Ar*

The measured reflectances at 1070 nm can be seen in table 4.3.

Temp	Reflectance at 1070 [nm]
600°C	61.19%
700°C	72.34%
800°C	83.87%

Table 4.3: *Reflectance at a wavelength of 1070 nm for sample 6-8*

As depicted in table 4.3 a general increase in reflectance can be seen in samples 7 and 8 as well.

Drude Lorentz Fit

The Drude–Lorentz model was applied to the reflectance spectrum of sample 6 using the parameters listed in 2.1. The resulting fit is shown in Fig 4.4.

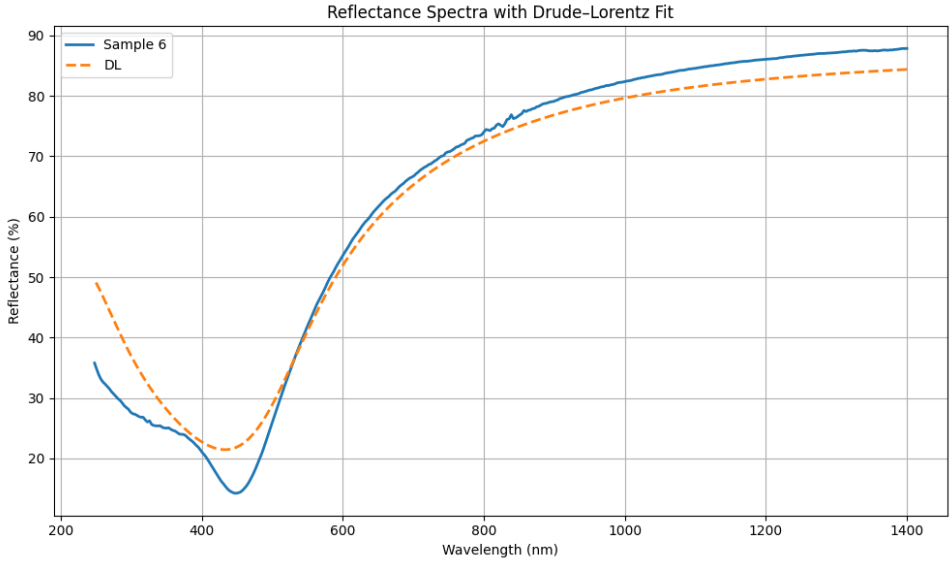

Figure 4.4: *Initial Drude–Lorentz fit to the reflectance spectrum of sample 6.*

The initial model fails to accurately capture the reflectance minimum associated with interband transitions. To improve the agreement between the model and the experimental data, the fitting parameters listed in table 2.1 were adjusted. The optimized parameters obtained from this fitting procedure are presented in table4.4.

ε_∞	$\omega_p\,(\mathrm{eV})$	$\Gamma_D\,(\mathrm{eV})$	$\omega_{L,1}^2\,(\mathrm{eV}^2)$	$\gamma_1\,(\mathrm{eV})$	$\omega_{0,1}\,(\mathrm{eV})$	$\omega_{L,2}^2\,(\mathrm{eV}^2)$	$\gamma_2\,(\mathrm{eV})$	$\omega_{0,2}\,(\mathrm{eV})$
6.78	8.10	0.49	85.00	1.10	5.00	5.38	1.82	1.84

Table 4.4: *Optimized Drude–Lorentz parameters for sample 6.*

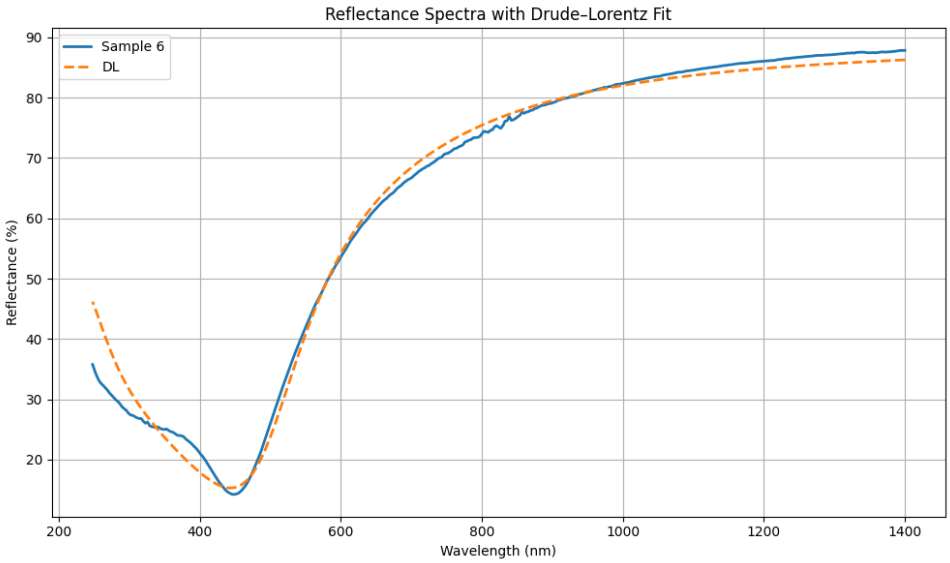

Figure 4.5: *Improved Drude–Lorentz fit to the reflectance spectrum of sample 6.*

The updated fitted model reproduces both the intraband response and interband transitions more accurately, with a notable improvement in the description of the interband transition. However, some differences remain in the interband transition region, indicating that the inclusion of a third Lorentz oscillator may be necessary to fit the reflectance minimum better.

4.1.2 AFM Analysis

All of the AFM scans in this project were performed according to section 3.4 and subsequently analysed using the Gwyddion software [49]. Processsing tools used were "Mean plane subtraction" to remove large-scale tilt from the height data and "align rows" with a polynomial of degree 2 to correct line-by-line height distortions by fitting and subtracting a smooth quadratic curve from each scan line. Additionally, the correcting horizontal scars setting was utilised for creating smoother image by adjusting sudden height jumps.

Surface Morphology

AFM scans were made for TiN coating deposited on the silicon substrates with different deposition temperatures. Figures 4.6 to 4.9 depict the AFM scans of samples 1-4 according to Table 3.1) respectively.

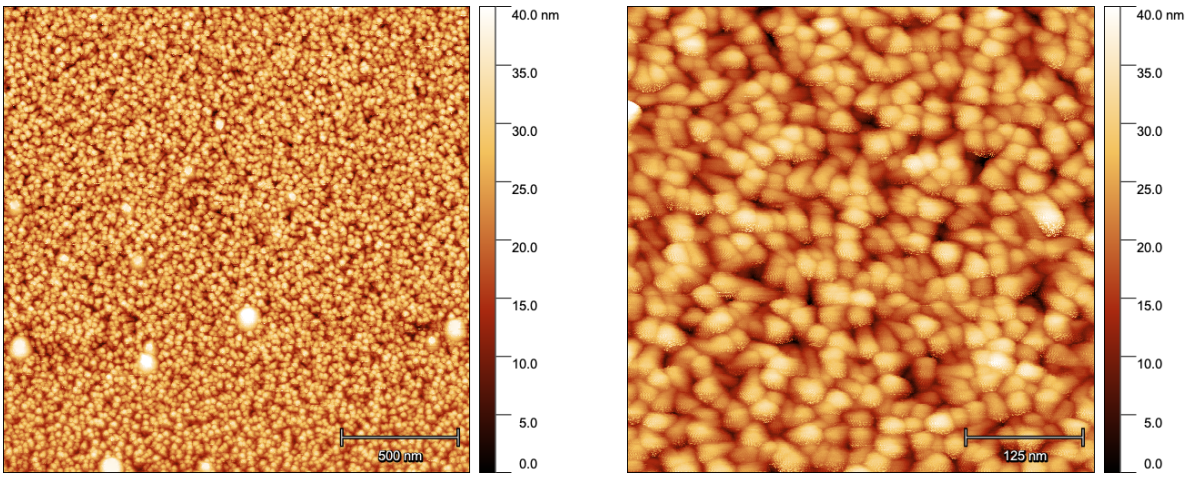

(a) **(b)**

Figure 4.6: *AFM scans of the TiN film on the silicon substrate deposited at 500°C with dimensions (a) 2x2 µm and (b) 0.5x0.5 µm.*

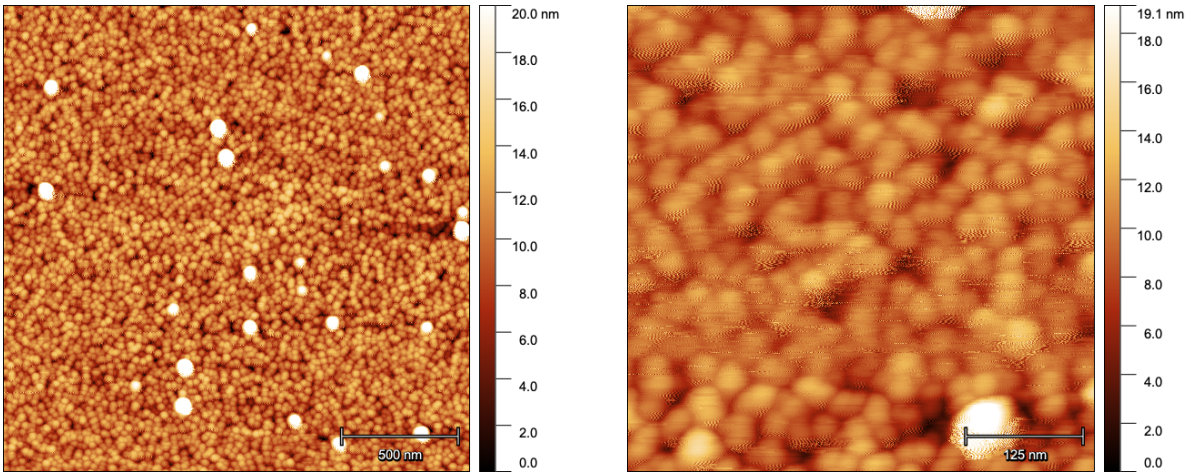

(a) **(b)**

Figure 4.7: *AFM scans of the TiN film on the silicon substrate deposited at 600°C with dimensions (a) 2x2 µm and (b) 0.5x0.5 µm.*

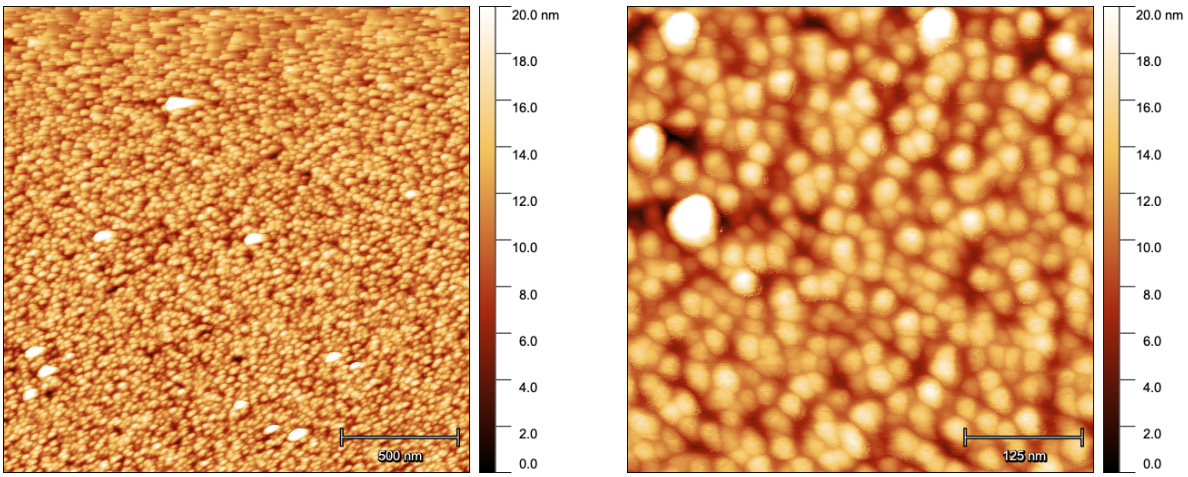

(a) **(b)**

Figure 4.8: *AFM scans of the TiN film on the silicon substrate deposited at 700°C with dimensions (a) 2x2 µm and (b) 0.5x0.5 µm.*

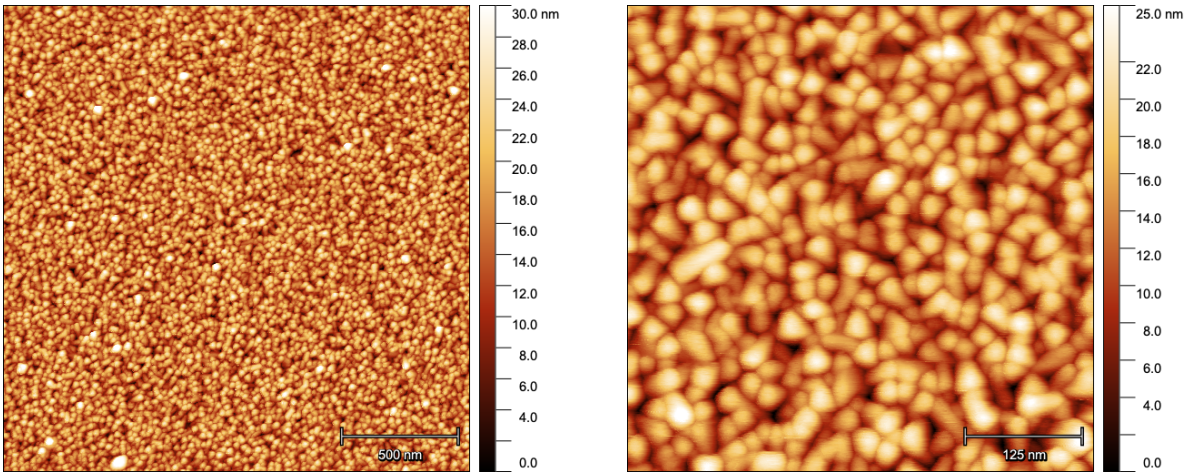

(a) **(b)**

Figure 4.9: *AFM scans of the TiN film on the silicon substrate deposited at 800°C with dimensions (a) 2x2 µm and (b) 0.5x0.5 µm.*

All the images illustrate a dense granular morphology with rounded grains. Figures 4.6a, 4.7a and 4.8a show the presence of abnormally large isolated features with significantly elevated height ranging from approximately 20-40 nm comparing to the surroundings. The mean diameter of these particles for each sample (1-4) was calculated using "Measure distances and directions between points" tool. Figure 4.10 depicts marked particles for the first sample and Table 4.5 presents the sizes of their diameters as an example. The same procedure was implemented for 2-4 samples. Table 4.6 displays the calculated mean diameter of the large features visible at the AFM pictures for each sample 1-4.

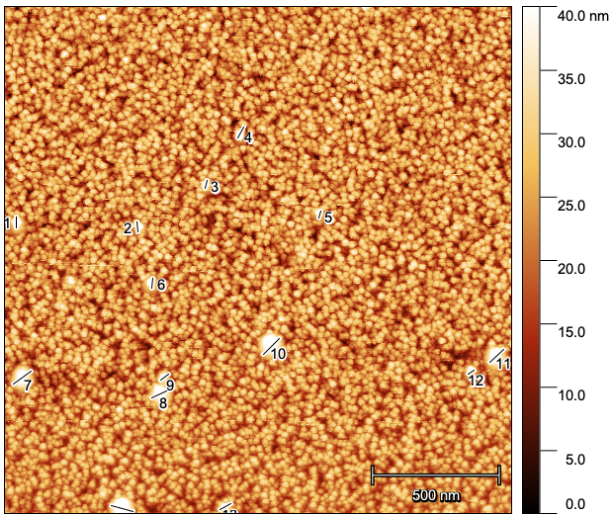

Figure 4.10: *Residual particles marked for mean diameter calculation for 500°C sample.*

Counts	1	2	3	4	5	6	7	8	9	10	11	12	13	14
Residual particle size (nm)	42.9	39.2	32.2	48.9	28.4	39.2	86.6	64.6	39.0	88.2	74.5	28.1	48.9	88.9

Table 4.5: *Diameters of marked residual particles for the first sample.*

Sample	1	2	3	4
Mean diameter (nm)	53.5	61.6	42.6	33.8

Table 4.6: *Mean diameter of abnormally high features for samples 1-4.*

As visible in Table 4.6, samples 1 and 2 contain wider features than samples 2 and 3. Additionally, sample 4 exhibits more uniform surface morphology. Figure 4.9a displays more consistent distribution of grain sizes across the larger area.

The presence of these impurities may be attributed to non-uniform growth processes inherent to reactive magnetron sputtering. Energetic ion bombardment during deposition promotes repeated nucleation and defects formation leading to variation in the local growth rates. Under these conditions, some regions of the film surface grow preferentially and develop with significantly greater height and lateral size compared to the surroundings [50] [51].

However, there are no direct studies, showing that surface morphology becomes more homogeneous at deposition above 800°C, it may be concluded that at higher deposition temperatures, enhanced adatom mobility and microstructural densification reduce the persistence of these growth anomalies, resulting in smaller and less pronounced surface features [50].

Grain Size

The 0.5x0.5 μm scans reveal the grain sizes more accurately, hence they were used to estimate them. The estimation was made by Gwyddion software. Initially, "mark grains by watershed" tool was used to optimally mark the grains within the scan. Subsequently, filtering grains by their properties tool was used to exclude the areas where grains were not split properly. Figures 4.11a to 4.11d present the mask applied to split the grains.

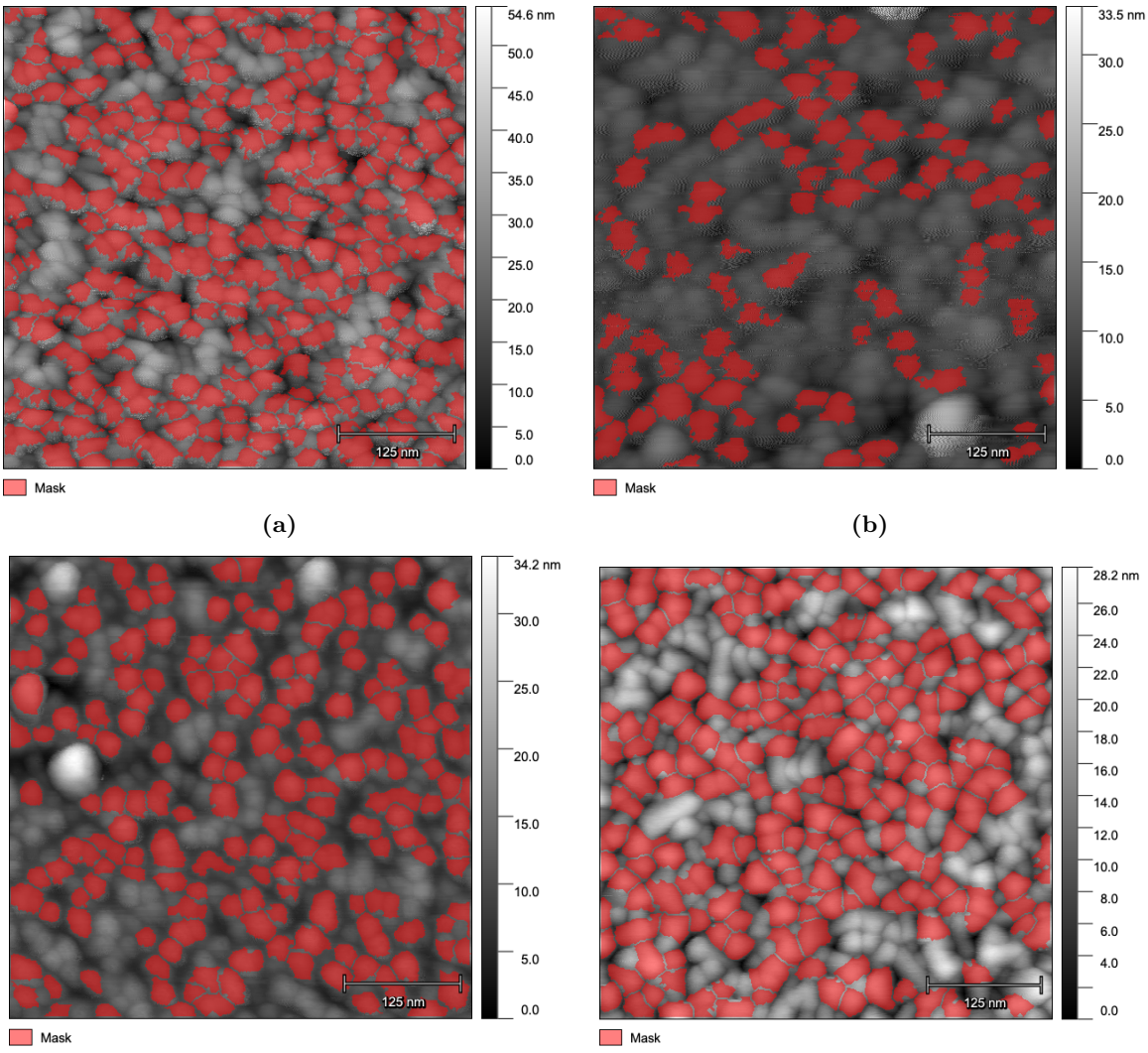

Figure 4.11: *Mask applied on the grains for the samples deposited at (a) 500°C, (b) 600°C. (c) 700°C and (d) 800°C.*

Having the mask, option of "distribution of various grain characteristics" was chosen and from "boundary" tab, mean radius was selected in order to obtain the data presenting the grain counts with corresponding radius measures. Graphs were plotted with changing radius to diameter for better analysis.

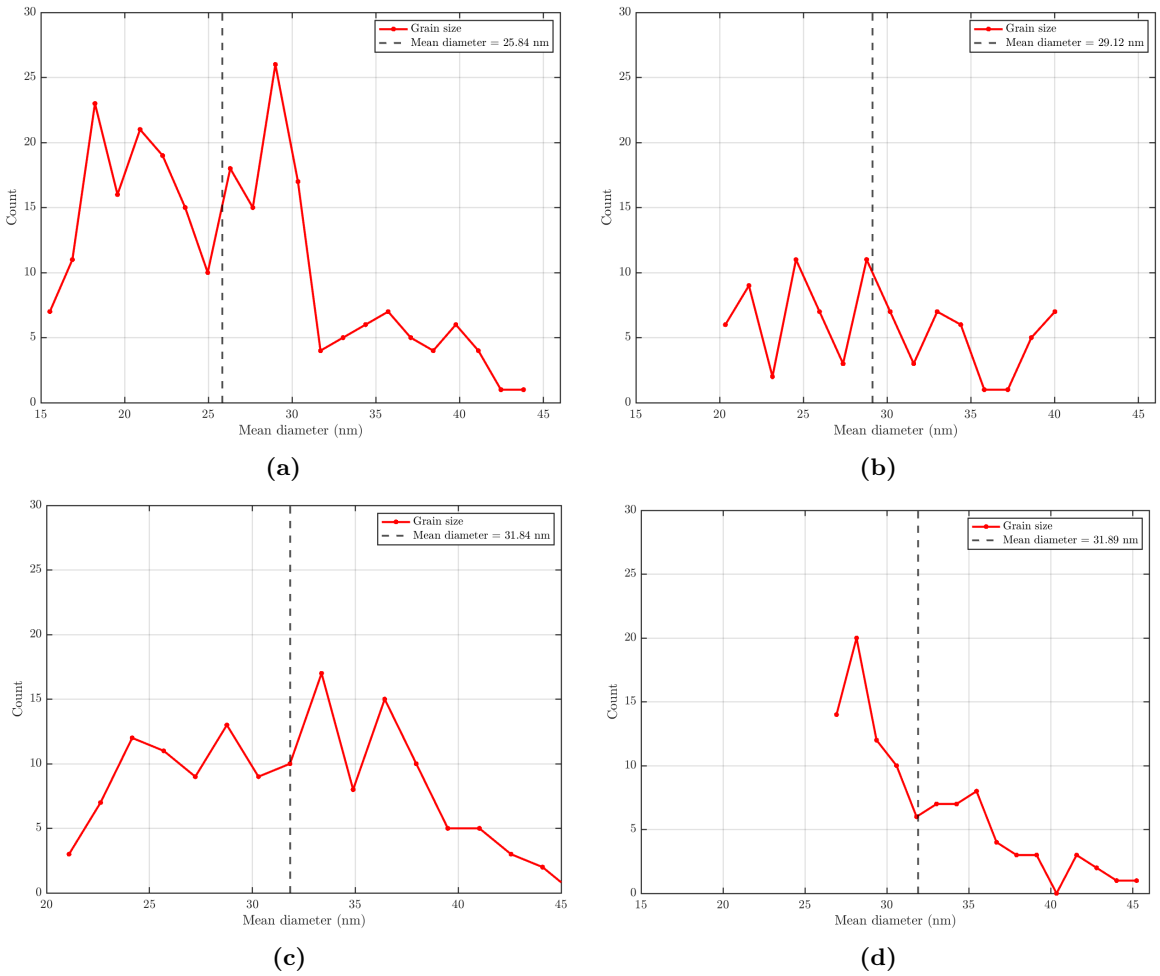

Figure 4.12: *Counts of grain with corresponding mean diameter for films deposited at 500°C, (b) 600°C. (c) 700°C and (d) 800°C.*

It is visible that the grain size is slightly increasing together with an increase in the growth temperature. The mean diameter of grains is 25.8, 29.12, 31.84 and 31.89 nm for the films deposited at 500, 600 ,700 and 800°C respectively.

The grain size shown in figures 4.11 and 4.12 demonstrates a clear dependence on the deposition temperature. As the temperature increases from 500 °C to 800 °C, the mean grain diameter increases from 25,8 nm to approximately 31,9 nm. Although the increase is gradual, the trend is consistent across all samples, showing that temperature plays a key role for the microstructral growth of the TiN films.

The grain masks presented in figure 4.11 show that films deposited at lower temperatures consist of more densely packed, smaller grains, whereas films grown at higher temperatures exhibit fewer but larger grains with more clearly defined boundaries. This observation could be also supported by the grain size distribution plots in figure 4.12, where the distribution shift toward larger diameters with increasing temperature. In particular, the distributions for the 700 °C and 800 °C samples show a broader tail toward larger grain diameters, indicating enhanced grain merging at higher temperatures.

The increase in grain size with temperature could be also explained by thermally activated

surface diffusion processes during the film growth. At higher substrate temperatures, adatoms possess thermal energy to diffuse over longer distances before incorporation into the lattice [52].

The relatively small difference in mean grain diameter between the samples deposited at 700 °C and 800 °C suggests that grain growth begins to saturate at higher deposition temperatures.

Surface Roughness

For the calculations of surface roughness the 2x2 μm scans were used. Surface roughness was measured by Gwyddion software after appropriate data processing. This processing included applying a mask and then marking data range in order to exclude abrupt changes in height from the roughness calculations, such as large surface features or artifacts. Figure 4.13 represents marked regions that were excluded from the AFM scan of the TiN film deposited at 600°C. The same procedure was conducted for other samples.

Subsequently, Statistical Quantities tool was used to check the mean roughness. Table 4.7 summarizes the RMS (root mean square) roughness values that were obtained for all samples, reporting results calculated both on the entire scanned area and on the region excluding the masked features.

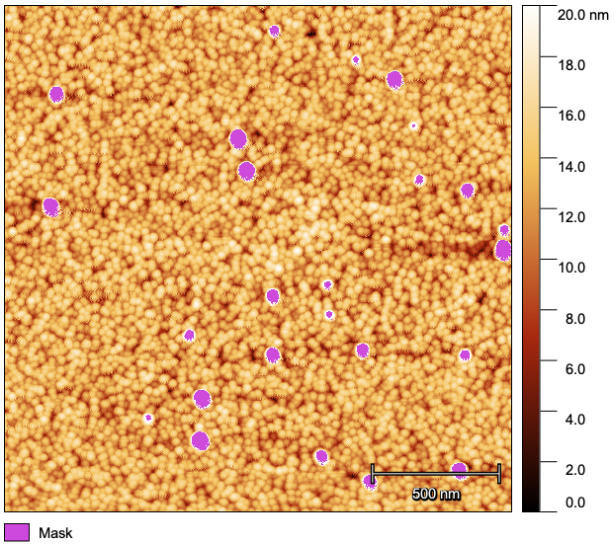

Figure 4.13: *Excluded regions for the roughness calculation of the TiN film deposited at 600°C.*

Samples	Temperature (°C)	RMS Roughness (nm) Exclude Masked Region	RMS Roughness (nm) Whole Region
Sample 1	500	3,961	4,495
Sample 2	600	2,383	2,940
Sample 3	700	2,404	2,584
Sample 4	800	4,216	4,419

Table 4.7: *RMS surface roughness as a function of temperature.*

The RMS surface roughness values seen in the table 4.7 show an overall increase with increasing deposition temperature, since observing that the TiN deposited at 800 °C exhibits a higher roughness compared to the film deposited at 500 °C. This behaviour is consistent with results

reported by M. R. Hantehzadeh et al [53] for thin films, where higher substrate temperatures promote grain growth and the formation of larger surface features, leading to increased height variations across the surface.

Although the roughness values for the films at 600 °C and 700 °C do not follow a strictly monotonic trend, such deviations could be from AFM-based roughness analysis. RMS roughness measurements may be sensitive to the scan area selection, but also to instrumental factors such as the cantilever geometry, tip etc. Furthermore, given that the roughness differences between these samples are on the nanometer scale, small variations in measurement conditions may result in shift in the calculated RMS values.

In addition, changes in crystal structure by higher temperature may also contribute to the observed roughness behavior without necessarily following a linear temperature dependence. Therefore, the non-monotonic roughness variation in this temperature range is considered physically reasonable.

It is important to note that all measured RMS roughness values remain within the nanometer range. At this scale, the roughness is significantly smaller than the wavelength of visible and near-infrared light, and therefore surface roughness is not expected to have an influence on the reflectance of the films.

It is important to note that M. R. Hantehzadeh et al. results are based on deposition temperatures lower than those used in the present study [53].In both low and high temperature regimes, increased temperature energy enhances adatom mobility, promotes grain growth, and leads to the development of more pronounced surface features. The observation of similar surface roughness at higher deposition temperatures suggests that temperature related grain growth continue to control the surface morphology [54].

4.1.3 Thickness Measurement

Thickness measurements were performed as described in section 3.2. Measurements were carried out on samples 4 and 6. Figures 4.14 and 4.15 show the measured EDS spectra and their corresponding Monte Carlo simulations. The legends in Figures 4.14b and 4.14c correspond to the total integrated intensity, absorbed or non absorbed, for each curve. The same applies to Figure 4.15. The absorbed intensity (which is what is simulated to be absorbed by the detector) from the simulation is used to compare intensity ratios with the experimental measurements. For both samples 4 and 6, the results with an beam energy of 10 keV and a working distance of 15 mm can be seen in figure 4.14, 4.15 and table 4.8.

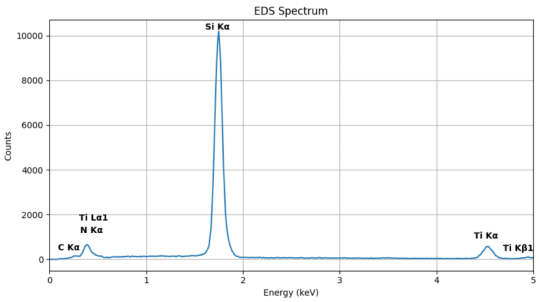

(a)

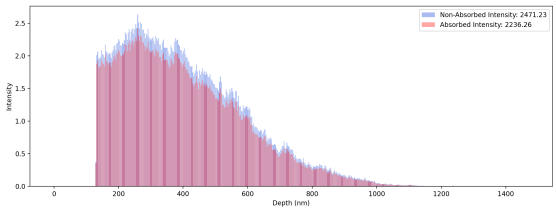

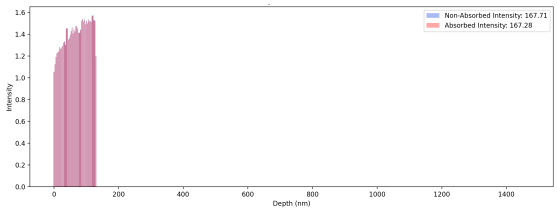

(b) **(c)**

Figure 4.14: *EDS spectrum and PRZ depth profiles for Si and Ti for sample 4*

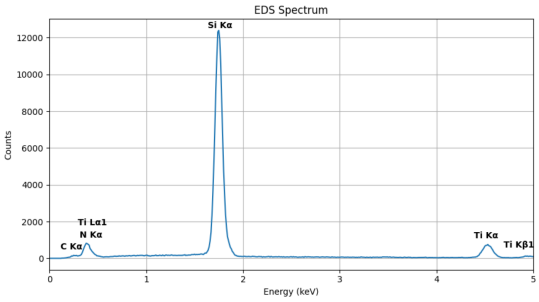

(a)

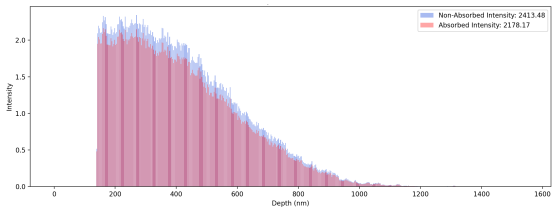

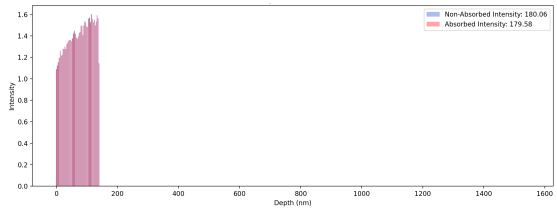

(b) **(c)**

Figure 4.15: *EDS spectrum and monte depth profiles for Si and Ti for sample 6*

The measured counts and ratio of Si Kα and Ti Kα counts, as well as the ratio of absorbed Si and Ti intensities from the Monte Carlo simulation and the corresponding estimated thickness are shown in Table 4.8.

Sample	Si kα counts	Ti kα counts	Ratio from measurement	Ratio from simulation	Estimated thickness (nm)
4	103434	7753	0.0749	0.0748	132
6	123182	10183	0.0826	0.0824	142 ± 2.5

Table 4.8: *Table describing the measured counts and ratio of Si Kα and Ti Kα counts and the ratio of absorbed Si and Ti intensities from the Monte Carlo simulation, including the estimated thickness.*

The results from a measurement with another beam energy of 9 keV and a working distance of 9mm for sample 4 and 18.91mm for sample 6 can be seen in the table below .

Sample	Si kα counts	Ti kα counts	Ratio from measurement	Ratio from simulation	Estimated thickness (nm)
4	108361	9559	0.0882	0.08678	131± 1
6	85358	8409	0.0985	0.0972	142 ± 2.5

Table 4.9

The thickness values estimated from the comparison between experimental EDS measurements and Monte Carlo simulation show a clear dependence on process pressure. For sample 4 the estimated film thickness increases from 131±1 nm to $142 \pm 2,5$ nm for sample 6, as the summarized table 4.8 shows. The reason for the thickness increase might be due to the lowered pressure as discussed earlier. Furthermore, in both cases, well defined Si Kα,Ti Kα and N Kα peaks are observed, confirming the presence of TiN thin film on the Si substrate.

This increase in thickness could be also accompanied by an increase in the measured Ti Kα counts, as the accelerating voltage and working distance were kept constant at 10 keV and 15 mm respectively. However, an increase in Si Kα counts was also be noticed from the figures 4.14a and 4.15a.

The observed thickness variation could be attributed to the lowered process pressure by lowered total gas flow. As mentioned on previous paragraphs a reduction in process pressure may lead to an increase in the mean free path of sputtered atoms, thereby reducing the number of collisions before the atoms reach the substrate. As a result, a higher fraction of sputtered atoms reaches the substrate, increasing the deposition rate and leading to thicker films [36].

To access the accuracy of the EDS thickness estimation, the results were compared with profilometry measurements performed on the Profiler: Ambios XP-2 on sample 4. The thickness obtained from there showed good agreement with the EDS Monte Carlo estimation.

4.2 Deposition on Graphite

In this section, results and discussion from the deposition on Graphite are presented.

Sample 9, which is TiN deposited on a graphite substrate, with the same parameters as sample 6, is seen in table 3.1.

4.2.1 Reflectance

Following the same procedure as on Si(100), reflectance was also measured on sample 9 to see the effect of a graphite substrate and the result can be seen in Figure 4.16.

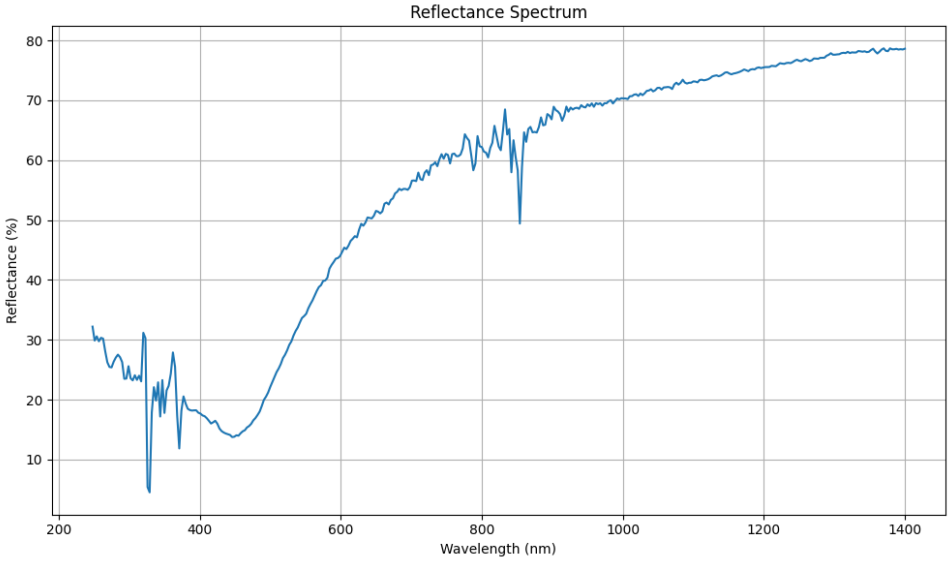

Figure 4.16: *Reflectance spectrum of sample 9*

Comparing the reflectance of sample 9, the curve generally follows the same form and shape as the other TiN samples, except that it has a higher reflectance minimum at around 450 nm. The associated interband transitions seem less distinct, as the reflectance curve is broader in that area compared to the other samples. The reflectance measured at 1070 nm is 72.23%, which is lower than what is measured for sample 6, even though the deposition parameters have been the same.

Indicating that a change of substrate, and therefore different TiN growth, might be the reason for the lower reflectance. The noise seen at around 330 nm and 850 nm is assumed to stem from the measurement itself.

4.2.2 Thickness Measurement

A thickness measurement has been done on sample 9 as well, with three different energies, as seen in Table 4.10. The measurement with a beam energy of 4 keV had a working distance of 18.91 mm, while the other two had the same working distance of 17 mm. Since some of the measurements were conducted at low energies (e.g. 4 and 5keV), Ti Kα peaks were not detected or were very low, and therefore the ratio of Ti Lα/C Kα was used for those energies.

EDS spectrum and a Monte Carlo simulation with the measurement conducted with a beam energy of 5 keV can be seen down below.

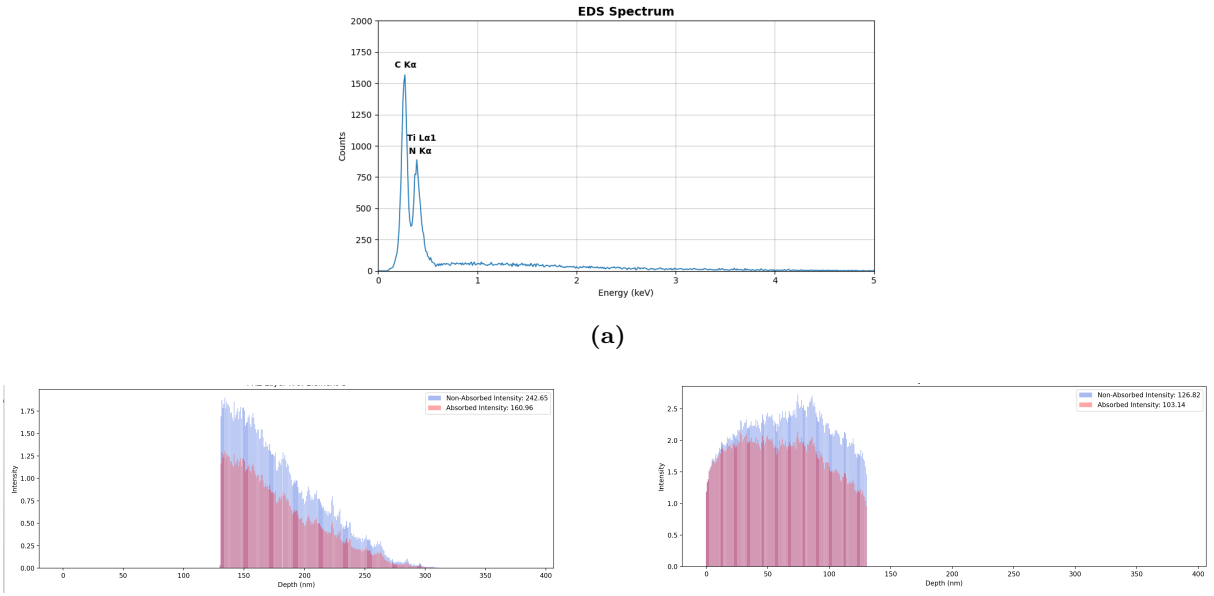

(a)

(b) **(c)**

Figure 4.17: *EDS spectrum and Monte Carlo depth profiles for C and Ti for sample 9*

Energy[keV]	C Kα counts	Ti Kα counts	Ti Lα counts	Ratio (measured)	Ratio (simulated)	Estimated thickness [nm]
4	4080	–	2776	0.6804	0.688	95 ± 0.5
5	10605	–	6816	0.6427	0.6495	131±1
10	21645	3372	1422	0.1558 & 0.0657	0.1553 & 0.0672	115 & 139± 1

Table 4.10

Three different estimated thicknesses were calculated from measurements at three different beam energies. The measurement conducted with a beam energy of 4 keV is not directly comparable to the other two, since it was performed at a different working distance.

There is still a fairly large difference between the thicknesses calculated from beam energies of 5 keV and 10 keV. One might suspect this difference arises from using Ti Lα instead of Ti Kα when calculating the ratio for the 5 keV measurement. Furthermore, at 10 keV a large difference is observed when the thickness is estimated using the Ti Lα/C Kα ratio compared to the Ti Kα/C Kα ratio.

Another explanation could be that, since the graphite surface is very rough (e.g. having large height variation), this might be the reason for the inconsistencies observed at different beam energies. As a result, no definitive conclusion can be drawn regarding the thickness of the TiN layer deposited on graphite.

4.2.3 Microscope images

All the images were taken by a AXIO Imager M2m microscope from Zeiss company with different magnifications ranging from 5x to 50x.

Figure 4.18a depicts graphite sample without TiN coating, whereas Figure 4.18b presents graphite sample with TiN coating.

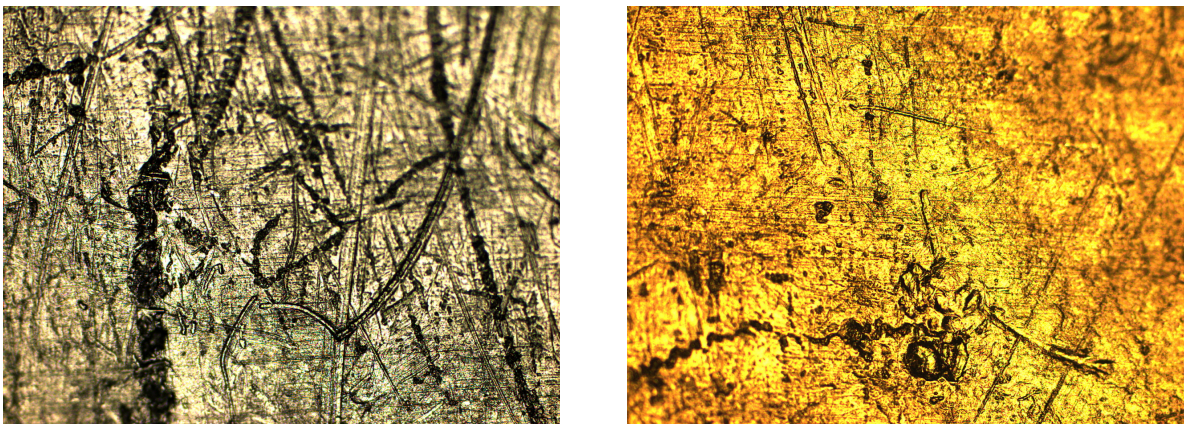

(a) (b)

Figure 4.18: *Microscope images of graphite samples with 10x magnification (a) without TiN coating (b) with TiN coating.*

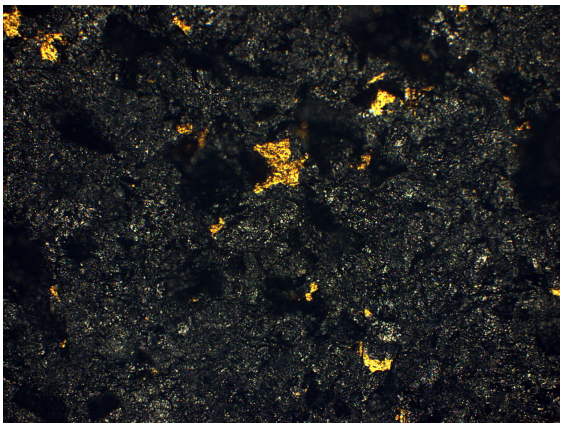

(a)

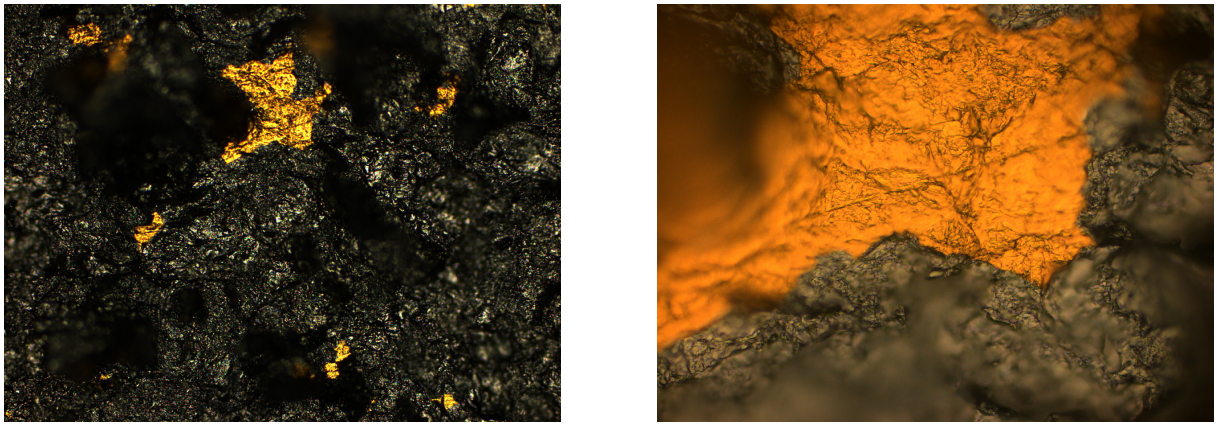

(b) (c)

Figure 4.19: *Microscope images of graphite samples after tape test with (a) 5x magnification (b) 10x magnification (c) 50x magnification.*

The colour difference between these two samples is substantial. Graphite substrate itself exhibits gray colour, while TiN coating yield with golden colour. This demonstrates that deposition of TiN on the graphite was successful. To analyse the adhesion of TiN to graphite, tape test was carried out, which was based on sticking the tape to the graphite sample with

the coating and removing it afterwards. Optical microscopy images acquired at 5x, 10x and 50x magnification are depicted in the Figure 4.19. As shown on the images, tape test resulted in the removal of TiN coating nearly entirely. There are still localized regions with the presence of the residual TiN, however they cover only a minor fraction of the tested area. Moreover, on the removed tape, thin layer of graphite was observed, which indicates that in many regions, material separation occurred within the graphite substrate rather than strictly between TiN and graphite interface. The results indicate stronger adhesion between the TiN coating and the graphite substrate, than between graphite interfaces. In addition, small amount of remaining TiN suggests non-uniform coating removal across the sample, likely due to local variations in substrate surface and coating properties or human error during tape removal.

4.3 Deposition on Carbon Fibers

In this section, results and discussion from the deposition on Carbon Fibers samples are presented.

The deposition of TiN on CF was done with substrate temperature reaching 500°C and Argon to Nitrogen flow 10:10 as presented in the Table 3.1.

4.3.1 Microscope images

All the images were taken by a AXIO Imager M2m microscope from Zeiss company as for the graphite sample with 50x magnification. Figure 4.20 depicts the CFs without coating, with TiN coating and after tape experiment respectively. Tape experiment, which was based on sticking the tape on CFs and removing it in order to analyse the coating-substrate adhesion.

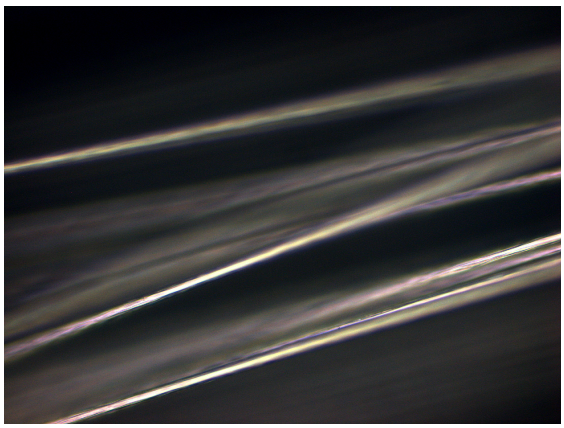

(a)

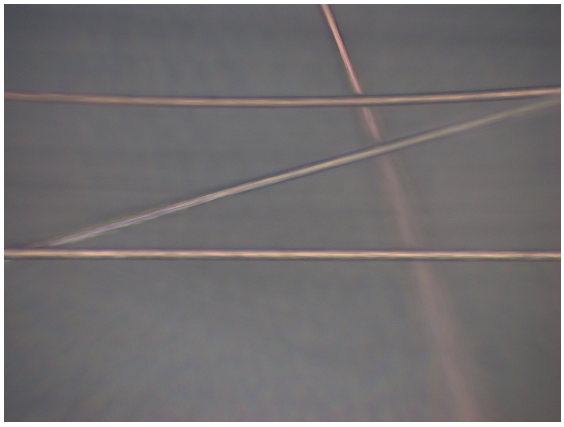

(b)

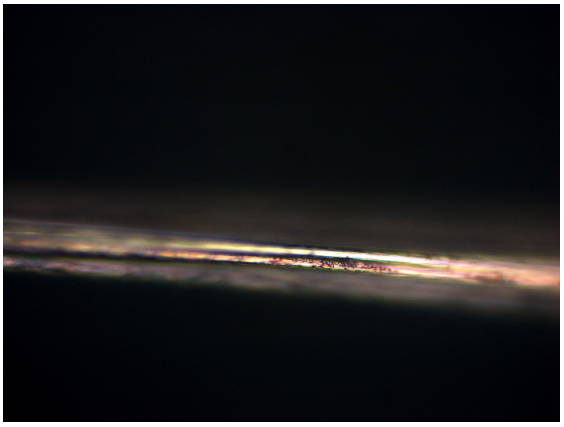

(c)

Figure 4.20: *Microscope images of Carbon Fibers (a) without TiN coating (b) with TiN coating (c) after taping.1*

The difference in colour for images in Figures 4.20a and 4.20b suggests that the coating was deposited with success, as CFs in Figure 4.20b are more gold. Distinct cracks are visible in Figure 4.20c, which might indicate that some of the TiN layer was removed and even the CFs itself undergone slight degradation. Nevertheless, from Figure 4.20c the adhesion between CFs and TiN coating cannot be clearly determined and compared to the adhesion between CFs interfaces.

Conclusion 5

It can be concluded that the temperature is identified as one of the most influential parameters for achieving high reflectance in TiN films. An increase in deposition temperature resulted in a moderate rise in reflectance at 1070 nm.

Nevertheless, the temperature is not the only parameter influencing the reflectance. Further improvements in reflectance were achieved by lowering the total gas flow, which reduced the process pressure during deposition.

The highest reflectance at 1070 nm for silicon substrate was achieved with a substrate temperature of 800°C and a process pressure of 1.49×10^{-2} mbar, with it reaching 83.87%.

The Drude Lorentz model was applied to sample 6, where the parameters were adjusted to fit the reflectance spectra measured. The fit did not completely match in the interband transitions region, indicating that a third lorentz oscillator might be needed.

AFM measurements made for samples with silicon substrates revealed that increase in temperature promotes grain growth and improves the uniformity of the films surface. At the same time, an overall increase in the RMS surface roughness was observed at higher temperatures, however all roughness values were ranging from approximately 2 to 4 nm and are therefore unlikely to affect reflectance in the visible and NIR wavelength range.

Thickness analysis using EDS and Monte Carlo simulations showed that lower process pressure led to increased film thickness because of an enhanced deposition rate. However, since the films are below the optically opaque after 90 nm, the observed increase in reflectance is more likely connected to improved microstructure rather than thickness effects alone.

When TiN films were deposited on graphite substrates, a reduced reflectance was observed compared to films grown on Si(100) yielding in 72.23% reflectance, despite identical deposition conditions. It is assumed that the substrate plays a role in determining the growth behaviour and optical performance of TiN films. However, further experiments have to be conducted in order to draw any conclusions on that matter. The thickness measurement carried out on graphite proved to be inconsistent and a specific one was not determined. Adhesion analysis revealed that material removal during tape tests occurred within the graphite substrate itself, suggesting stronger adhesion between TiN and graphite rather than graphite interfaces.

TiN deposition on CFs proved to be successful. Optical microscope images after executing tape tests showed significant cracks on the CFs, however it is unclear whether only the TiN layer was removed or CFs and TiN together. Therefore,no conclusion on the adhesion of TiN and CFs interface can be drawn.

Bibliography

[1] A. Abidin et al. "Preparation and characterization of CVD-TiN-coated carbon fibers for applications in metal matrix composites". In: *Thin Solid Films* 589 (2015), pp. 479–486. ISSN: 0040-6090. DOI: https://doi.org/10.1016/j.tsf.2015.06.022. URL: https://www.sciencedirect.com/science/article/pii/S004060901500629X.

[2] K. Pooja, N. Tarannum, and P. Chaudhary. "Metal matrix composites: revolutionary materials for shaping the future". In: *Discover Materials* 5 (Feb. 2025). DOI: 10.1007/s43939-025-00226-6.

[3] S. Seetharaman and M. Gupta. "Additive Manufacturing of Metal Matrix Composites". In: Jan. 2021. ISBN: 9780128035818. DOI: 10.1016/B978-0-12-819724-0.00099-9.

[4] P. Norman et al. "Incorporation of CNT-yarns into metals by laser melting of powder". In: Sept. 2012. DOI: 10.2351/1.5062416.

[5] A. Ureña et al. "Effect of copper electroless coatings on the interaction between a molten Al–Si–Mg alloy and coated short carbon fibres". In: *Composites Part A: Applied Science and Manufacturing* 38.8 (2007), pp. 1947–1956. ISSN: 1359-835X. DOI: https://doi.org/10.1016/j.compositesa.2007.02.005. URL: https://www.sciencedirect.com/science/article/pii/S1359835X07000255.

[6] B. Brandau et al. "Absorbance study of powder conditions for laser additive manufacturing". In: *Materials & Design* 216 (2022), p. 110591. ISSN: 0264-1275. DOI: https://doi.org/10.1016/j.matdes.2022.110591. URL: https://www.sciencedirect.com/science/article/pii/S026412752200212X.

[7] H. Honda and M. Watanabe. "Quantifying Laser Absorptivity of Ti–6Al–4V Powder through Additive Manufacturing Systems". In: *MATERIALS TRANSACTIONS* 65.2 (2024), pp. 194–198. DOI: 10.2320/matertrans.MT-M2023156.

[8] D.-H. Kuo and K.-W. Huang. "Kinetics and microstructure of TiN coatings by CVD". In: *Surface and Coatings Technology* 135.2 (2001), pp. 150–157. ISSN: 0257-8972. DOI: https://doi.org/10.1016/S0257-8972(00)00986-5. URL: https://www.sciencedirect.com/science/article/pii/S0257897200009865.

[9] S. B. Ghantasala and S. Sharma. "Magnetron Sputtered Thin Films Based on Transition Metal Nitride: Structure and Properties". In: *physica status solidi (a)* 220.2 (2023), p. 2200229. DOI: https://doi.org/10.1002/pssa.202200229. eprint: https://onlinelibrary.wiley.com/doi/pdf/10.1002/pssa.202200229. URL: https://onlinelibrary.wiley.com/doi/abs/10.1002/pssa.202200229.

[10] S. B. Ghantasala and S. Sharma. "Magnetron Sputtered Thin Films Based on Transition Metal Nitride: Structure and Properties". In: *physica status solidi (a)* 220.2 (2023), p. 2200229. DOI: https://doi.org/10.1002/pssa.202200229. eprint: https://onlinelibrary.wiley.com/doi/pdf/10.1002/pssa.202200229. URL: https://onlinelibrary.wiley.com/doi/abs/10.1002/pssa.202200229.

[11] H. O. Pierson. "Handbook of Refractory Carbides and Nitrides". In: 1996. ISBN: 978-0-8155-1392-6. DOI: https://doi.org/10.1016/B978-081551392-6.50001-5.

[12] P. Patsalas, N. Kalfagiannis, and S. Kassavetis. "Optical Properties and Plasmonic Performance of Titanium Nitride". In: *Materials* 8.6 (2015), pp. 3128–3154. ISSN: 1996-1944. DOI: 10.3390/ma8063128. URL: https://www.mdpi.com/1996-1944/8/6/3128.

[13] F. Mehmood et al. "Electronic and optical properties of titanium nitride bulk and surfaces from first principles calculations". eng. In: *Journal of applied physics* 118.19 (2015). ISSN: 0021-8979.

[14] A. Catellani and A. Calzolari. "Plasmonic properties of refractory titanium nitride". In: *Physical review. B* 95.11 (2017), pp. 115145–. ISSN: 2469-9950.

[15] H. Reddy et al. "Temperature-Dependent Optical Properties of Plasmonic Titanium Nitride Thin Films". eng. In: *ACS photonics* 4.6 (2017), pp. 1413–1420. ISSN: 2330-4022.

[16] F. Pedrotti, L. Pedrotti, and L. Pedrotti. *Introduction to Optics*. Cambridge University Press, 2017. ISBN: 9781108428262. URL: https://books.google.dk/books?id=06o_DwAAQBAJ.

[17] A. G. Isaev and A. E. Rogozhin. "Structure of Thin Films of Titanium Nitride Formed by Magnetron Sputtering". eng. In: *Russian microelectronics* 54.3 (2025), pp. 265–274. ISSN: 1063-7397.

[18] K. W. Kolasinski. *Surface science: foundations of catalysis and nanoscience*. John Wiley & Sons, 2020.

[19] S. R. Singamaneni et al. "Ferromagnetic oxide heterostructures on silicon". In: *MRS Communications* 6.3 (2016), pp. 234–240.

[20] R. Machunze and G. Janssen. "Stress and strain in titanium nitride thin films". In: *Thin Solid Films* 517.20 (2009), pp. 5888–5893. ISSN: 0040-6090.

[21] K. S. Harsha. *Principles of vapor deposition of thin films*. Elsevier, 2005.

[22] H. Wang et al. "Epitaxial growth of TaN thin films on Si (100) and Si (111) using a TiN buffer layer". In: *Applied physics letters* 80.13 (2002), pp. 2323–2325.

[23] A. Obraztsov et al. "Chemical vapor deposition of thin graphite films of nanometer thickness". In: *Carbon* 45.10 (2007), pp. 2017–2021. ISSN: 0008-6223. DOI: https://doi.org/10.1016/j.carbon.2007.05.028. URL: https://www.sciencedirect.com/science/article/pii/S0008622307002965.

[24] H. Ameen and S. Wilayat. "In situ synthesis of oxidation and wear resistant coatings on graphite". In: *2019 16th International Bhurban Conference on Applied Sciences and Technology (IBCAST)* (2019), pp. 92–99. URL: https://api.semanticscholar.org/CorpusID:84187317.

[25] M. Mahmood et al. "Development and Characterization of Oxidation Resistant TiC Coating on Graphite". In: *2019 16th International Bhurban Conference on Applied Sciences and Technology (IBCAST)*. 2019, pp. 30–34. DOI: 10.1109/IBCAST.2019.8667140.

[26] K. Ronoh et al. "Comprehensive characterization of different metallic thin films on highly oriented pyrolytic graphite substrate". In: *Vacuum* 215 (2023), p. 112345. ISSN: 0042-207X. DOI: https://doi.org/10.1016/j.vacuum.2023.112345. URL: https://www.sciencedirect.com/science/article/pii/S0042207X23005420.

[27] A. not listed. "Carbon fibres: Effect of various thermo-oxidative environments on structural and performance damage". In: *Carbon* (2025). Describes carbon fiber manufacturing from PAN and oxidation behavior above 550 °C.

[28] B. I. (of carbon fiber oxidation onset and temperatures). *Is Carbon Fiber Heat Resistant?* Details oxidation onset above 500 °C and degradation of properties. 2025. URL: https://biologyinsights.com/is-carbon-fiber-heat-resistant/.

[29] E. KIM. *Carbon Fiber: A Comprehensive Overview*. Discusses oxidation of carbon fiber in air beginning around 400–600 °C. 2025. URL: https://erickimphotography.com/carbon-fiber-a-comprehensive-overview/.

[30] O. O. Abegunde et al. "Overview of thin film deposition techniques". In: *AIMS Materials Science* 6.2 (2019), pp. 174–199. ISSN: 2372-0484. DOI: 10.3934/matersci.2019.2.174. URL: https://www.aimspress.com/article/doi/10.3934/matersci.2019.2.174.

[31] K. Ø. Simonsen and V. D. Andersen. *Embedding Carbon Fibres in Ti6Al4V using Selective Laser Melting*. Aarhus University, 2025.

[32] D. Mattox. "Handbook of Physical Vapor Deposition (PVD) Processing". In: *Metal Finishing* 98 (Jan. 2000). DOI: 10.1016/S0026-0576(00)80350-5.

[33] S. A. Campbell. *Fabrication Engineering at the Micro and Nanoscale*. 2007. URL: https://api.semanticscholar.org/CorpusID:108838711.

[34] N. Jain et al. *Metal Deposition: Plasma-Based Processes*. Taylor and Francis, New York (USA), Jan. 2016, p. 19. DOI: 10.1081/E-EPLT-120053919.

[35] K. Seshan. "Handbook of Thin Film Deposition Processes and Techniques: Principles, Methods, Equipment and Applications". In: 2001. URL: https://api.semanticscholar.org/CorpusID:91314039.

[36] M. Ohring. *Materials Science of Thin Films - Deposition and Structure (2nd Edition)*. eng. 2nd ed. San Diego ; Tokyo: Elsevier, 2002. ISBN: 0125249756.

[37] A. Shugurov, E. Kuzminov, and A. Panin. "The effect of substrate bias on the structure, mechanical and tribological properties of DC magnetron sputtered Ti-Al-Ta-Si-N coatings". In: *Surface and Coatings Technology* 517 (2025), p. 132858. ISSN: 0257-8972. DOI: https://doi.org/10.1016/j.surfcoat.2025.132858. URL: https://www.sciencedirect.com/science/article/pii/S0257897225011326.

[38] D. L. Smith and D. W. Hoffman. "Thin-Film Deposition: Principles and Practice". eng. In: *Physics today* 49.4 (1996), pp. 60–62. ISSN: 0031-9228.

[39] S. Massahi et al. *The effect of deposition process parameters on thin film coatings for the Athena X-ray optics*. eng. Vol. 11822. SPIE, 2021, 118220B-118220B–10. ISBN: 1510644822.

[40] R. Hill. "Thin film phenomena: K.L. Chopra, published by McGraw-Hill, New York, 1969; 1135 pages; price: 235". eng. In: *Thin Solid Films* 5.3 (1970), pp. 199–199. ISSN: 0040-6090.

[41] D. M. Mattox. *Handbook of Physical Vapor Deposition (PVD) Processing (2nd Edition)*. eng. 2nd Edition. Kidlington, Oxford: Elsevier, 2010. ISBN: 9780815520375.

[42] B. Gadagi and R. Lekurwale. "A review on advances in 3D metal printing". In: *Materials Today: Proceedings* 45 (2021). 4th International Conference on Advanced Research in Mechanical, Materials and Manufacturing Engineering-2020, pp. 277–283. ISSN: 2214-7853. DOI: https://doi.org/10.1016/j.matpr.2020.10.436. URL: https://www.sciencedirect.com/science/article/pii/S2214785320380573.

[43] B. Gadagi and R. Lekurwale. "A review on advances in 3D metal printing". In: *Materials Today: Proceedings* 45 (2021). 4th International Conference on Advanced Research in Mechanical, Materials and Manufacturing Engineering-2020, pp. 277–283. ISSN: 2214-7853. DOI: https://doi.org/10.1016/j.matpr.2020.10.436. URL: https://www.sciencedirect.com/science/article/pii/S2214785320380573.

[44] N. S. S. AG. *Ti6al4v grade 23 eli astm b348/ astm f136/ astm f3001 material data sheet. Technical report, SLM Solutions, Estlandring 4, 23560 Lübeck,Germany,n.d.* SLM Solutions, 2025. URL: https://www.slm-solutions.com/fileadmin/Content/Powder/MDS/nw/nw2024/mds5137.pdf.

[45] J. Stoever. "Defect related transport mechanism in the resistive switching materials SrTiO3 and NbO2". In: (Aug. 2021). DOI: 10.18452/23122.

[46] J. Sotelo, J. Ederth, and G. Niklasson. "Optical properties of polycrystalline metallic films". In: *Phys. Rev. B* 67 (19 May 2003), p. 195106. DOI: 10.1103/PhysRevB.67.195106. URL: https://link.aps.org/doi/10.1103/PhysRevB.67.195106.

[47] Q. Ma et al. "Influence of the deposition temperature on the optical and electrical properties of TiN film by spectroscopic ellipsometry". In: *Superlattices and Microstructures* 151 (2021), p. 106815. ISSN: 0749-6036. DOI: https://doi.org/10.1016/j.spmi.2021.106815. URL: https://www.sciencedirect.com/science/article/pii/S0749603621000136.

[48] R. Secondo et al. "Reliable modeling of ultrathin alternative plasmonic materials using spectroscopic ellipsometry [Invited]". In: *Optical Materials Express* 9 (Jan. 2019), pp. 760–770. DOI: 10.1364/OME.9.000760.

[49] D. Nečas and P. Klapetek. "Gwyddion: an open-source software for SPM data analysis". In: *Central European Journal of Physics* 10 (1 2012), pp. 181–188. ISSN: 1895-1082. DOI: 10.2478/s11534-011-0096-2.

[50] F. Magnus et al. "Morphology of TiN thin films grown on SiO2 by reactive high power impulse magnetron sputtering". In: *Thin Solid Films* 520.5 (2011). 38th International Conference on Metallurgical Coatings and Thin Films (ICMCTF 2011), pp. 1621–1624. ISSN: 0040-6090. DOI: https://doi.org/10.1016/j.tsf.2011.07.041. URL: https://www.sciencedirect.com/science/article/pii/S0040609011014283.

[51] V. Chawla, R. Jayaganthan, and R. Chandra. "Structural characterizations of magnetron sputtered nanocrystalline TiN thin films". In: *Materials Characterization* 59.8 (2008), pp. 1015–1020. ISSN: 1044-5803. DOI: https://doi.org/10.1016/j.matchar.2007.08.017. URL: https://www.sciencedirect.com/science/article/pii/S1044580307003026.

[52] A. Jamnig et al. "Atomic-scale diffusion rates during growth of thin metal films on weakly-interacting substrates." In: *Scientific Reports* 9.1 (2019).

[53] M. R. Hantehzadeh et al. “The effect of substrate temperature on the structure and morphology of titanium nitride compounds grown by DC magnetron sputtering”. In: *Journal of fusion energy* 30.4 (2011), pp. 333–337.

[54] L. Du et al. “AFM study on the surface morphologies of TiN films prepared by magnetron sputtering and Al2O3 films prepared by atomic layer deposition”. In: *Vacuum* 153 (2018), pp. 139–144. ISSN: 0042-207X. DOI: https://doi.org/10.1016/j.vacuum.2018.04.004. URL: https://www.sciencedirect.com/science/article/pii/S0042207X17310941.

Appendix A

A.1 Generative AI Declaration

Use of Generative AI (GAI) in This Project

GAI has been used in this project to support the writing and review process.

Models Used

- GPT-5.1
- GPT-5.2

How GAI Was Used

- Alternative ways of formulating text
- To check spelling and grammar